ERASMUS MUNDUS JOINT MASTER DEGREE IN NUCLEAR PHYSICS

****

UNIVERSIDAD COMPLUTENSE DE MADRID

FACULTAD DE CIENCIAS FÍSICAS

Master's Thesis

NuWro SIMULATION OF FINAL STATE INTERACTIONS IN QUASIELASTIC NEUTRINO-NUCLEUS SCATTERING

CARLISLE AURABELLE M. CASUGA

Supervisors

JOSÉ MANUEL UDÍAS

RAÚL GONZÁLEZ JIMÉNEZ

September 2021

To my advisers, Jose Manuel and Raul, thank you for all the help and guidance, in this thesis, in this manuscript and in the defense. I also humbly dedicate this work and the work I've done in this masters to Mama, Joven, and my dear friends and family back home.

Pauwi na ako Ma, ihanda niyo na yung sinigang.

Abstract

The collaboration of the theoretical and experimental aspects of the study of neutrino oscillation is crucial to the success of the detection of neutrinos and measurement of oscillation parameters. Monte Carlo event generators serve as a bridge between these two sectors, where nuclear models from theory are used to extrapolate experimental data. Therefore, the improvement of the implementation of nuclear models on these generators are important. This thesis aims to contribute to this by studying NuWro's simulation of the charged current quasielastic scattering of a neutrino on a nucleon. In experiments, this nucleon is bound to a nucleus. Nuclear effects should, therefore, be accounted for. In this thesis, the Relativistic Fermi Gas model and the Spectral Function approach in modelling the initial state of the nucleon is studied. Cross sections that are calculated for these models are then compared to that of NuWro's simulation. Through this, nuclear effects like Pauli Blocking, short range correlations, binding energy, and Fermi motion is explored. The main goal, however, is to study NuWro's cascade model, that simulates the Final State Interactions, where the outgoing nucleon re-interacts with the residual system. This is studied through cross section calculations of different final states that shed light to the probability of a certain interaction to happen in the cascade. Numerous observations were made about nucleon-nucleon and pion-nucleon interactions in the cascade. This thesis then compared NuWro calculations with sophisticated theoretical calculations that use phenomenological optical potentials in a fully quantum and relativistic mean field setup. This comparison highlighted possible improvements that could be made to NuWro's cascade model.

Contents

List of Figures

iv

Acronyms

CC Charged Current.

CCQE Charged Current Quasielastic.

DIS Deep Inelastic Scattering.

DUNE Deep Underground Neutrino Experiment.

FD Far Detector.

FG Global Fermi Gas.

FSI Final State Interactions.

IA Impulse Approximation.

INC IntraNuclear Cascade.

LAr liquid argon.

LArTPC LAr Time Projection Chamber.

LFG Local Fermi Gas.

MC Monte Carlo.

MEC meson exchange current.

NC Neutral Current.

ND Near Detector.

NN nucleon-nucleon.

PB Pauli Blocking.

piN pion-nucleon.

PMNS Pontecorvo, Maki, Nakagawa, Sakata.

QE QuasiElastic.

RES Resonance Production.

RFG Relativistic Fermi Gas.

ROP Relativistic Optical Potential.

RPWIA Relativistic Plane Wave Impulse Approximation.

rROP Real Relativistic Optical Potential.

SF Spectral Function.

SK Super-Kamiokande.

SM Standard Model.

SRC short range correlation.

T2K Tokai-to-Kamiokande.

1   Significance and Outline of Study

Neutrinos are invisible and elusive. To detect and characterize them, experiments rely on its limited interaction with matter via the weak force. Among the channels in the neutrino-nucleus scattering, the Charged Current Quasielastic (CCQE) reaction is dominant in the energy region of interest of long baseline neutrino experiments. CCQE is when a neutrino (antineutrino) interacts with a neutron (proton) and produces a charged lepton of the same flavor as the original neutrino and a proton (neutron). When the nucleon is bound to a nucleus, the incoming neutrino would, occasionally, interact with a correlated pair of nucleons producing an additional nucleon from the CCQE vertex. The lepton usually easily escapes and could be detected; however, the nucleon/s undergo further nuclear effects as they traverse the nuclear medium. They can either be absorbed by the nucleus, can produce hadrons, mostly pions, can also change in charged state, or interact elastically with the other nuclear constituents. These are called Final State Interactions (FSI) and they contribute a significant change to the momenta of the final nucleons.

One main hurdle of neutrino experiments is that the incoming neutrino energy can only be estimated indirectly through what is seen by the detector. This reconstruction relies on the information of the particle configuration in the nuclei and the dynamics of the nucleons inside the target nucleus. The FSI and nucleon correlation models and this information on particle configuration are what comprise a nuclear model. This nuclear model is relevant in many parts of a neutrino oscillation experiment. In the near detector, the event topology of the neutrino beam is determined through the measurement of the momenta of the final state particles from its reaction with the target in the detector. The energy and flux of the neutrino beam is found through fine tuning nuclear model parameters implemented in a Monte Carlo (MC) event generator to match the previously said event topology. This nuclear model comes into play again at reconstructing events at the far detector where oscillation parameters can then be estimated from.

MC event generators implement nuclear models to simulate the momentum distribution of the final state particles from the interaction of neutrinos and the target. This information, along with data on the cross sections of different neutrino - bound nucleon interaction, is used to break down the detector response to reconstruct the previously unknown incoming neutrino beam energy.

The purpose of this thesis is to perform a qualitative study of the nuclear models implemented in NuWro, a neutrino event generator developed by theorists in Poland. The study aims to calculate differential cross sections of different configurations of the final state particles produced by the neutrino-nucleus interaction. Furthermore, the study aims to compare these cross section calculations done by NuWro with that done by theoretical models. However, the main objective of the study is to examine the final state interaction model of NuWro, what is called the cascade model, and study its effect on the momentum of the final state particles, especially of the leading nucleon. The study will be focusing on the CCQE channel only.

With these objectives in mind, the next chapter, Chapter 2, starts the thesis off with an introduction on neutrino oscillation and neutrino oscillation experiments. Chapter 3 continues by detailing the cross section formalism focusing on the CCQE interaction. Further into the chapter, CCQE interaction is expanded on by discussing the the CCQE-like neutrino - nucleus interaction and by introducing nuclear models, like the Spectral Function (SF) and the Relativistic Fermi Gas (RFG). Included in this chapter are cross section calculations using these nuclear models in comparison to corresponding NuWro calculations. Chapter 4 gives an introduction to MC event generators and NuWro. This chapter contains the bulk of the results of this study, presenting different NuWro cross sections for different final states. It includes assessment on the effects of final state interactions on proton momenta through NuWro's cascade model. Comparisons of these cross section to quantum models of the FSI are also presented. Chapter 5 concludes this manuscript with a summary.

2   Introduction to Neutrinos and Neutrino Oscillation

2.1   History of Neutrinos

The necessity for the existence of the neutrino started when the energy spectrum of an electron emitted in beta decay was examined. If the beta decay were a two body decay, meaning $(A, Z) \rightarrow (A, Z + 1) + e^-$, the spectrum should be a discrete line; however, experiments obtained a continuous spectrum indicative of a missing varying energy carried by a third particle.

In 1930, this particle was hypothesized by Wolfgang Pauli as an unknown light particle, ν, initially called it "neutron", as a "desperate remedy" [1] to explain this continuous spectrum to save the law of conservation of energy. Further problems were solved by Enrico Fermi in 1934 when he theorized a new fundamental interaction. Fermi assumes that the number of electrons and the, now-called, neutrinos do not have to be constant and that the proton and (the actual) neutron are two different states of the same particle. It was Fermi who coined the name neutrino was given [1].

Numerous questions still remain unanswered: the difference of neutrino from the anti-neutrino, and the measurement of the mass of this very light particle. Bethe and Peierls [2] hypothesized that if Fermi is right, then the creation of neutrinos implies the existence of an annihilation process. Most interestingly, it is the inverse beta day where the neutrino disappears after it interacts with a nucleus and produces an electron or a positron.

Processes like the beta decay, however, have very small cross sections. It took around twenty years for the technology to catch up to solve this problem, which is through producing larger detectors or higher neutrino fluxes. Even then, scientists still find the difficulty of neutrino detection very challenging, with some experiment having to wait 90 days but no activity detected. But by 1945, Pontecorvo has showed that experimental

observation of the beta decay is "not out of the question". He then proposes to exploit the reaction [3]:

$$\nu + {}^{37}\text{Cl} \rightarrow {}^{37}\text{Ar} + e^- \qquad (2.1)$$

where, the half-life of ^{37}Ar was sufficiently long to be a candidate. Louis Alvarez [1] then continues to fully develop this into a complete experimental proposal. By studying past Cl-Ar experiments, he developed models to account for different background sources and found that experiments must be performed underground to lessen cosmic ray background. This experiment would be done by Raymond Davis in 1958 with a 0.8W power reactor. Eventually, with the onset of liquid scintillators and the reactor source used by Davis, the electron antineutrino was discovered by Reines and Cowan [4] via the $\bar{\nu}_e + p \rightarrow n + e^+$ using a Cd-doped water target.

In 1937, Ettore Majorana proposes an idea through modified Fermi theory involving the neutrino being its own antiparticle [5]. The mass of the neutrino remains in question. The symmetry breaking mechanism for the Standard Model (SM) gives mass to all the SM particles, however, excludes the neutrinos. SM consider the neutrinos to be massless. But neutrinos do in fact have mass, but so small that it would be very difficult to measure. Numerous experimental bounds have been set. The KATRIN experiment [6] measures the neutrino mass through the β decay of molecular tritium and set an upper limit of 1.1 eV.

Another major question on neutrinos was how many neutrino families there are. Around 1950, in the study of cosmic muon decay, two neutral particles were found as a product of the decay. By 1959, Pontecorvo formulates the first proposal for an experiment to search for the ν_μ and $\bar{\nu}_\mu$. The full experiment leading to the discovery of the second neutrino came at 1962 by Schwartz [7]. By the 1990s, the number of neutrino families, $N_\nu = 3$, are known thanks to the study of the virtual Z boson decay, $Z \rightarrow \bar{\nu}\nu$ at the Large Electron Positron Collider (LEP) [8]. The third neutrino, ν_τ, was discovered

by year 2000 by K. Niwa and collaborators [9] in Fermilab.

Going back to the 1957 Davis experiment, results of the confirmation of the existence of the $0\nu2\beta$ decay reached Pontecorvo and he said in a statement that it indicates the possibility that the neutrino charge is not strictly conserved. If the process is observed, Pontecorvo postulated that it might be due to antineutrinos transforming into neutrinos. With the discovery of the second and third neutrino families, he developed the modern theory of neutrino transformation in vacuum in 1968, fortified by the introduction of mixing between different families of neutrinos by Maki, Nakagawa, Sakata [10] in 1962. This phenomenon is called neutrino oscillation, which will be discussed in the following sections.

2.2   Neutrino Oscillation

2.2.1   Oscillation Probability

To reiterate, the idea of oscillation is first proposed by Pontecorvo. Eventually, the phenomena of neutrino oscillation becomes one proof of the non-zero mass of the neutrinos. The fundamental idea behind neutrino oscillation is the mixing of neutrino flavor states and neutrino mass states. The mixing is defined by an $N \times N$ unitary leptonic mixing matrix,

$$\nu_\alpha = \sum_{i=1}^{N} U_{\alpha i} \nu_i \ \text{ with } \begin{cases} \alpha = e, \mu, \tau & \text{[flavor]} \\ i = 1, 2, 3 & \text{[mass]} \end{cases} \tag{2.2}$$

where N is the number of neutrino families. These mass states have their own corresponding m_i mass. For $N = 3$, there is a total of 4 free parameters, of which there is one physical phase factor. The Pontecorvo, Maki, Nakagawa, Sakata (PMNS) matrix conventionally writes these parameters into mixing angles θ_{12}, θ_{13}, and θ_{23} and the CP

violating phase δ,

$$U_{PMNS} = \begin{pmatrix} c_{12}c_{13} & s_{12}c_{13} & s_{13}e^{-i\delta} \\ -s_{12}c_{23} - c_{12}s_{23}s_{13}e^{i\delta} & c_{12}c_{23} - s_{12}s_{23}s_{13}e^{i\delta} & s_{23}c_{13} \\ s_{12}s_{23} - c_{12}c_{23}s_{13}e^{i\delta} & -c_{12}s_{23} - s_{12}c_{23}s_{13}e^{i\delta} & c_{23}c_{13} \end{pmatrix}, \qquad (2.3)$$

where $c_{ij} = \cos\theta_{ij}$ and $s_{ij} = \sin\theta_{ij}$.

To be able to determine the values of these parameters, *disappearance* and *appearance* experiments are done. Disappearence experiments measure the survival of a certain neutrino flavor from a source; meanwhile, appearance experiments measure the *appearance* of a new neutrino flavor that is not present in the source, originally. These measurements is related to the oscillation probability that is a function of the PMNS parameters. To demonstrate this connection between the oscillation probability and the neutrino mixing parameters, we start with a simplification to only a two flavor case with 2×2 mixing matrix. First, the relation between neutrino flavor eigenstates and mass eigenstates is expressed as

$$|\nu_\alpha\rangle = \sum_i U_{\alpha i} |\nu_i\rangle. \qquad (2.4)$$

The mixing matrix is written as

$$U = \begin{pmatrix} \cos\theta & \sin\theta \\ -\sin\theta & \cos\theta \end{pmatrix}. \qquad (2.5)$$

Consequently, there is only one mixing angle for this matrix. Consider a neutrino produced in the Sun. Neutrinos in the Sun are produced in a specific flavor state, the electron neutrino flavor state. Neutrino mixing says that flavor states can be expressed as linear combinations of the mass states. For a 2 - flavor case,

$$|\nu_e\rangle = |\nu(t=0, x=0)\rangle = \cos\theta |\nu_i\rangle + \sin\theta |\nu_2\rangle \qquad (2.6)$$

As it propagates through space and travels a distance, this state evolves as

$$|\nu(L)\rangle = e^{-i\frac{m_1^2 L}{2E}} \cos\theta |\nu_1\rangle + e^{-i\frac{m_1^2 L}{2E}} \sin\theta |\nu_2\rangle, \qquad (2.7)$$

where m_1 and m_2 is the mass of ν_1 and ν_2, respectively, and $E_1 = E_2 = E$. The probability of detecting an electron neutrino, or the survival probability, is then

$$P_{ee} = |\langle \nu_e | \nu(L) \rangle|^2 \tag{2.8}$$

$$= |(\cos\theta \langle \nu_1| + \sin\theta \langle \nu_2|)(e^{-i\frac{m_1^2 L}{2E}} \cos\theta \, |\nu_1\rangle + e^{-i\frac{m_2^2 L}{2E}} \sin\theta \, |\nu_2\rangle)|^2 \tag{2.9}$$

$$= 1 - \sin^2(2\theta) \sin^2\left(\frac{\Delta m^2}{2E} L\right), \tag{2.10}$$

where the mass difference is $\Delta m^2 = m_1^2 - m_2^2$. The probability of detecting a muon neutrino, or the oscillation probability, instead, is

$$P_{\mu e} = |\langle \nu_\mu | \nu(L) \rangle|^2 = 1 - P_{ee}. \tag{2.11}$$

More generally, for N number of neutrino flavors,

$$P_{\alpha\beta} = \delta_{\alpha\beta} - 4 \sum_i \sum_{i<j} Re[U_{\alpha i}^* U_{\beta i} U_{\alpha j} U_{\beta j}^*] \sin^2\left(\frac{\Delta m_{ij}^2}{4E} L\right)$$
$$+ 2 \sum_i \sum_{i<j} Im[U_{\alpha i}^* U_{\beta i} U_{\alpha j} U_{\beta j}^*] \sin\left(\frac{\Delta m_{ij}^2}{2E} L\right), \tag{2.12}$$

where α is the production state, β is the detection state, and $\Delta m_{ij}^2 \equiv m_i^2 - m_j^2$.

2.2.2   Oscillation Parameters

The masses of the neutrino flavors enter the general oscillation probability in Equation 2.12 as the differences of their squared values. It is this parameter that is probed and not the individual mass values. The convention is that, for three neutrino families, $m_1 > m_2$ and that the smallest mass splitting is Δm_{12}^2, where

$$|\Delta m_{21}^2| \leq |\Delta m_{31}^2|, |\Delta m_{32}^2| \tag{2.13}$$

which demonstrates that there are two options, called hierarchies, between normal hierarchy and inverted hierarchy. For a normal hierarchy, $m_3 > m_2 > m_1$; otherwise, for an inverted hierarchy, $m_2 > m_1 > m_3$. Pictorially, this is demonstrated in Figure 1.
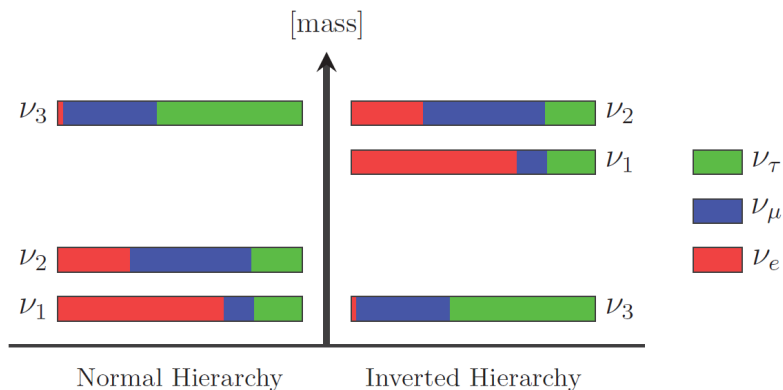
Figure 1: Mass hierarchy between flavor and mass states. This also demonstrates the mixing between flavor and mass states [1].

The PMNS matrix in Equation 2.3 is the result of 5 other phases being removed through the transformation

$$U_{\alpha k} = e^{i\theta_\alpha} U_{\alpha k} e^{i\theta_k}, \qquad (2.14)$$

leaving only the one phase, δ. This transformation leaves the oscillation probability invariant and leaves us with one phase that affects this probability.

In summary, 6 total parameters can be probed through neutrino oscillation probability measurements: two squared mass splittings Δm_{21}^2, and Δm_{31}^2, three mixing angles, θ_{12}, θ_{13}, and θ_{23}, and one phase angle, δ.

2.2.3   Oscillation length scale and regimes

The PMNS parameters can be probed at different regimes. For a mixing of two neutrino flavors, the survival and oscillation probabilities can be redefined by introducing the characteristic length scale,

$$L_{osc} \equiv 4\pi \frac{E}{\Delta m^2} \simeq 2.5\text{m} \left(\frac{E}{1MeV} \right) \left(\frac{eV^2}{\Delta m^2} \right),$$
(2.15)

where E and L can be adjust adjusted according to the experiment. The new probabilities is now

$$P_{ee} = 1 - \sin^2 (2\theta) \sin^2 \left(\pi \frac{L}{L_{osc}} \right),$$
(2.16)

and,

$$P_{e\mu} = \sin^2 (2\theta) \sin^2 \left(\pi \frac{L}{L_{osc}} \right).$$
(2.17)

This means that the probability oscillates as a function of the propagation length; more specifically when $L = [0, 1, 2, 3...] \cdot L_{osc}$ there is no oscillation but when $L = [\frac{1}{2}, \frac{3}{2}, \frac{5}{2}, ...] \cdot L_{osc}$, there is maximum oscillation.

At the limit $L \gg L_{osc}$, there have been so many oscillations happening in between the neutrino's trajectory that the second sine function in Equations 2.16 and 2.17 can be averaged . When $L \ll L_{osc}$, there is no oscillation. In summary, for these cases, the survival probability is

$$Pee \simeq \begin{cases} 1 & L \ll L_{osc} \\ 1 - \frac{1}{2} \sin^2 (2\theta) & L \gg L_{osc} \\ 1 - \sin^2 (2\theta) \sin^2 \left(\frac{\Delta m^2}{4E} L \right) & L \sim L_{osc} \end{cases}$$
(2.18)

The survival probability for the first two regimes have no dependence on energy so to probe the energy dependence, an experiment must cover the regime where $L \sim L_{osc}$.

2.3   Neutrino Oscillation Experiments

2.3.1   Neutrino Sources

Solar Neutrinos

Solar neutrinos are byproducts of nuclear reactions in the Sun to produce its energy. In the hydrogen burning phase, four protons are converted to helium via

$$4p \rightarrow {}^4\text{He} + 2e^+ + 2\nu_e + Q, \tag{2.19}$$

where Q is the energy released through photons or other products, where 2 electronic neutrinos are released. The majority reaction channel of reaction 2.19 is the *pp* chain: $p + p \rightarrow \nu_3 + d + e^+$, while the rest is produced in the CNO cycle. Breakdowns of both channels are shown in Figure 2. There is, however, the so-called *solar neutrino problem*, which is the deficit of flux signal [11] compared with expectations where the ν_e signal seems to be suppressed by some process in its propagation, later discovered to be the electronic neutrino's oscillation to ν_μ. Eventually, the further resolution of this problem comes from the Mikheyev–Smirnov–Wolfenstein (MSW) effect, a resonance enhancement of oscillations as the neutrino propagates in matter, in this case the solar medium. This effect accounted for the deficit in solar neutrino in certain ranges of the oscillation parameters.

With the propagation length being around $L \sim 10^8$ km and with energies around $E \sim 10^{-3} - 10^{-2}$, experiments sensitive to detecting solar neutrinos, can probe the mass splitting $\Delta m_{12}^2 = \Delta m_{\text{solar}}^2$ and mixing angle $\theta_{12} = \theta_{\text{solar}}$. Experiments like the Homestake experiment pioneered solar neutrino flux measurements. Meanwhile for the solar neutrino problem, after the publishing of the first Super-Kamiokande (SK) results, the MSW explanation became the more favored on. Decisive results came from SNO [11]. However, it is the KamLAND experiment [12] that offered a unique solution to this solar neutrino problem and successfully probed $\Delta m_{\text{solar}}^2$. This was done by by producing electron neu-

trinos and antineutrinos through several nuclear reactor sources. And these results were in agreement with the MSW explanation. Historically, this identification of the MSW solution provided the first correct evaluation of the neutrino oscillation parameters [1].
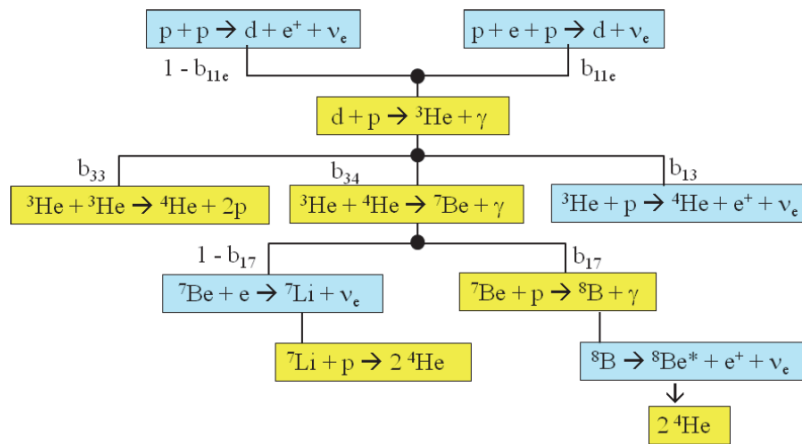
Figure 2: How electron neutrinos are produced through the pp-chain [1].

Modern experiments that will detect solar neutrinos, like the Hyper-Kamiokande in Japan, DUNE in the United States, SNO+ in Canada, will continue to address challenges like the measurement of $pp-$, $pep-$ and ^{7}Be fluxes, probe of matter effects in oscillation, testing new neutrino oscillation theories, and many more.

Atmospheric Neutrinos

Atmospheric neutrinos are produced via decay of secondary particles like pions, kaons, and muons, produced when cosmic rays interact with molecules in the Earth's atmosphere. More specifically, they come from decay channels like

$$\pi^{\pm}, K^{\pm} \rightarrow \mu^{\pm}\nu_{\mu}(\overline{\nu}_{\mu}) \tag{2.20}$$

$$\mu^{\pm} \rightarrow e^{\pm}\nu_{e}(\overline{\nu}_{e})\overline{\nu}_{\mu}(\nu_{\mu}) \tag{2.21}$$

$$K^{\pm}, K^{0}_{L} \rightarrow [\pi^{\pm}, \pi^{0}]e^{\pm}\nu_{e}(\overline{\nu}_{e}) \tag{2.22}$$

This regime covers the $\sim 10^{4}$ km propagation length range and $1 - 10$ GeV neutrino energy range, and here electronic and muonic neutrino types can be detected. The first indication of neutrino oscillation in this sector was found by the Kamiokande using a Cherenkov detector, where the $\frac{\nu_{\mu}}{\nu_{e}}$ flux detected were much less than expected. Even stronger evidence of oscillation was reported by the SK experiment, a successor of the Kamiokande experiment, sporting a larger volume Cherenkov detector complex. Because the ν_{e} oscillations were not detected, the muonic neutrino oscillation were attributed to ν_{τ}, where the tauonic neutrino often goes undetected. Through this muonic neutrino deficit, the mass splitting $\Delta m^{2}_{32} \approx \Delta m^{2}_{31} = \Delta m^{2}_{atm}$ and mixing angle $\theta_{31} \approx \theta_{32} = \theta_{atm}$ can be probed.

Reactor and Accelerator Neutrinos

While the $\Delta m^{2}_{\text{atm}}$ and θ_{atm} can be probed by experiments that are sensitive to atmospheric neutrinos, it is the reactor and long-baseline neutrino experiments that successfully measured the θ_{atm}. This mixing angle governs the neutrino oscillation in the framework of the three-flavor oscillation model.

Reactors are powerful sources of electronic antineutrinos, produced at a rate $\sim 10^{21}$ GWth (per second per gigawatt of reactor thermal power) through fission of ^{235}U, ^{239}Pu, ^{241}Pu, and ^{238}U. The neutrinos produced here have a mean energy of 3 MeV. A reactor based experiment is essentially a disappearance experiment, meaning the survival of electronic antineutrinos are counted at a far detector, $\sim 1 - 2$ km from the source. For this regime, the survival probability sheds light on the θ_{13} mixing angle. Examples of these reactor

experiments that measured this angle and provided a bound to it are the Double CHOOZ experiment in France and the Daya Bay experiment and RENO experiment in South Korea.

The oscillation measured by reactor experiments have dependence on fewer parameters than that measure by accelerator experiments. It doesn't depend on the violating phase, δ, and is, therefore, the more direct way of measuring θ_{13}. Meanwhile, it is the accelerator experiments that can probe this charge-parity violating phase.

The neutrinos accelerators produce are mainly muonic antineutrinos. Experiments like this are sensitive to the $\bar{\nu}_\mu \to \bar{\nu}_e$ oscillation channel. These are usually long-baseline experiments with oscillation length range, $L \sim 10^3$ km, and with neutrino energies, $E \sim 10$ GeV. It is in this range where the CCQE channel can be dominant, and the next section will be reserved to discuss these experiments in more detail.

In summary, the results and values of the oscillation parameters are presented in Table 1.

	θ_{12}	θ_{13}	θ_{23}	$\Delta m_{21}^2/10^{-5}$	$\Delta m_{3j}^2/10^{-3}$	δ
Normal hierarchy	$33.56^{+0.77}_{-0.75}$	$8.46^{+0.15}_{-0.15}$	$41.6^{+1.5}_{-1.2}$	$7.50^{+0.19}_{-0.17}$	$2.524^{+0.039}_{-0.040}$	261^{+51}_{-59}
Inverted hierarchy	$33.56^{+0.77}_{-0.75}$	$8.49^{+0.15}_{-0.15}$	$50.0^{+1.1}_{-1.4}$	$7.50^{+0.19}_{-0.17}$	$-2.514^{+0.038}_{-0.041}$	277^{+40}_{-46}

Table 1: Summary of results on Oscillation Parameters [6]. The values for Δm_{3j}^2 corresponds to Δm_{31}^2 for normal hierarchy and Δm_{32}^2 for inverted hierarchy.

2.3.2   Neutrino Detection

Neutrino detection, just like any detection of other particles, rely on the neutrinos' interaction with matter. This interaction can either be a Charged Current (CC) interaction by the exchange of a $W^\pm$ boson or a Neutral Current (NC) interaction by the exchange

of a Z boson. A CC interaction produces a charged lepton of the same flavor as the original neutrino. Meanwhile, the NC interaction has a neutrino with the original flavor coming out of the NC vertex. The Feynman diagrams of the two reactions are shown in Figure 3. When it comes to neutrino interaction with a nucleon, these interactions can be further broken down to three main channels according to the magnitude of the momentum transfer: the QuasiElastic (QE), the Resonance Production (RES), and the Deep Inelastic Scattering (DIS). A neutrino detector is designed to look for and measure the kinematics of the secondary particles that these reaction produce and reconstruct the incoming neutrino state from it.
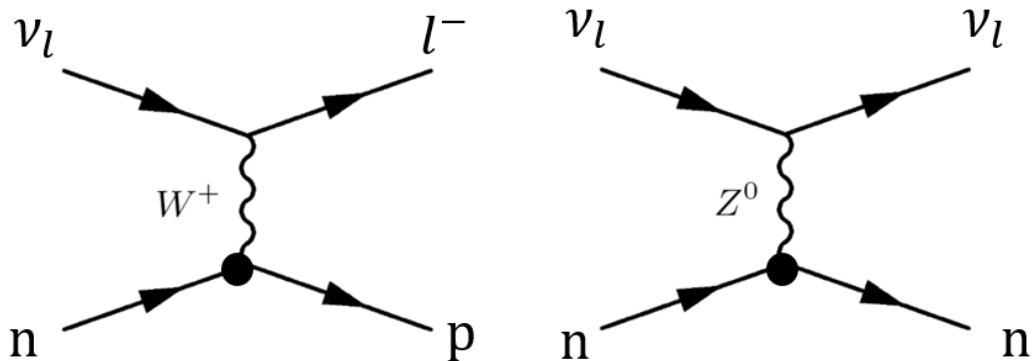
Figure 3: Feynman diagrams of CC (left) and NC (right) scattering for neutrinos.

A detector is designed according to the energy range to be probed, the level of neutrino flavor discrimination to be achieved, and the resolution on the measurement of the parameters needed. Because of the tiny cross section of the weak interaction, collecting statistically sound neutrino event data requires a large target volume. High energy resolution is achieved only through fully active detectors, where the interaction and detection functionality are fulfilled by a single homogeneous target medium that is either water, a liquid scintillator, or liquid argon (LAr).The resolution is further improved by detectors with finely segmented medium readout to allow tracking the secondary particles

produced in the neutrino interaction. Through these secondary and final state particles, initial parameters like neutrino energy can be reconstructed.

The CC neutrino interactions allow for the tagging of the incoming neutrino flavor by identifying the final state lepton: μ, e, or τ. For disappearance experiments, this capability is exploited by employing two identical detectors to measure the flux of the neutrino beam, before (Near Detector (ND)) and after (Far Detector (FD)) possible oscillation. Usually, the FD is placed at a propagation length, L, where the oscillation is significant or at a maximum.
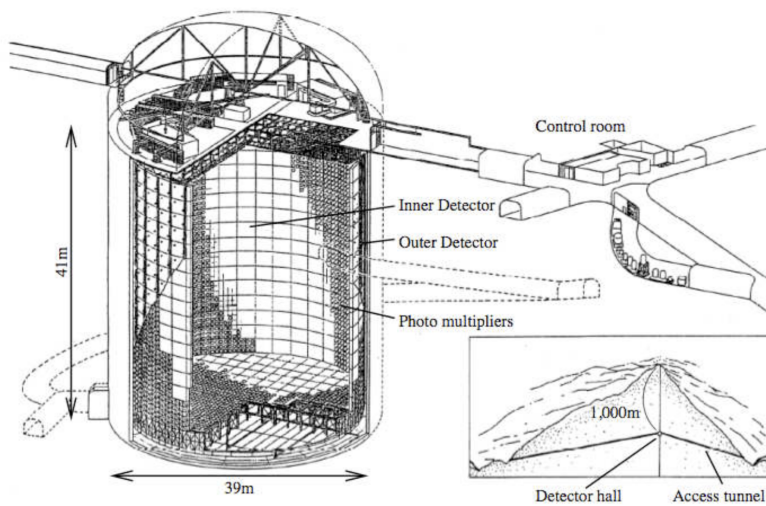
Figure 4: Diagram of Basic Set-Up of Super-Kamiokande Far Detector for the T2K Experiment [13].

Cherenkov detectors made possible the massive scaling up of neutrino experiments. These detectors are capable of discriminating between a muonic and an electronic neutrino signal. The T2K experiment sports the SK detector as its FD, as shown in Figure 4. It is a 50-kton water Cherenkov detector, cylindrical in shape. Its inner cylinder contains the active pure water target covered by ~ 11000 20-inch diameter photo-multiplier

tubes (PMTs). When a neutrino interacts with the target detector, emitted charged particles produced Cherenkov photons as it travels toward the PMTs at speeds larger than the speed of light in water. These photons project a ring of light on the walls of the detector, sampled by the array of PMTs. For electronic neutrinos, the electrons create electromagnetic showers and this manifests as a fuzzier light ring, as shown in Figure 5.
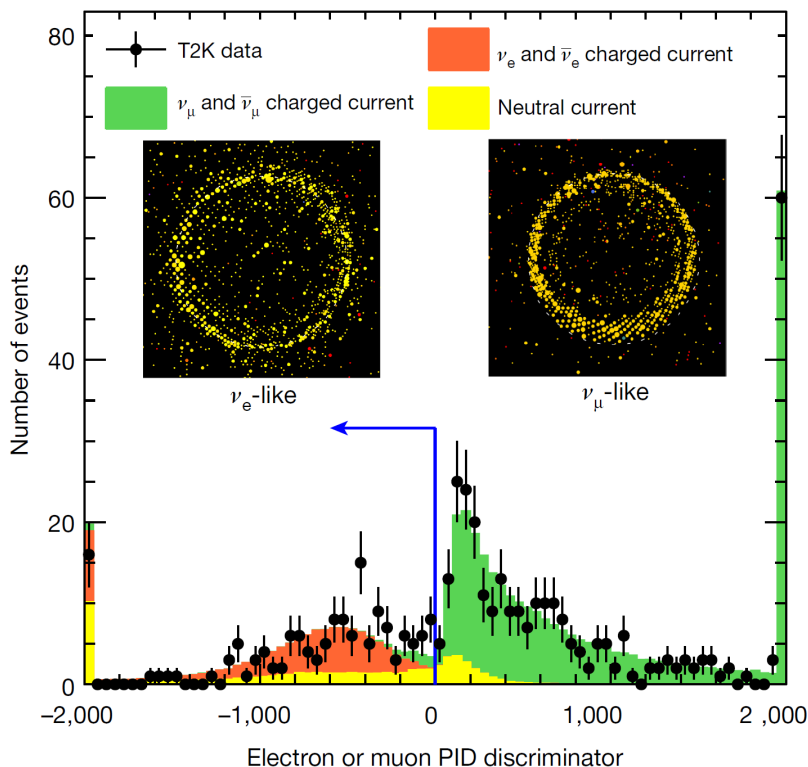
Figure 5: Spectrum of the particle identification parameter (PID) used to determine whether the Cherenkov rings are either electron-like and muon-like [13].

Another example of neutrino detector is the LAr Time Projection Chamber (LArTPC) detector [14]. The neutrino event signal is read in an anode plate located in one side of the detector. Here, electrons from the ionization made by secondary particles are collected. They reach the plate after a drift path traveled at constant velocity. This drift is made

by exposing the target volume in an electric field. Meanwhile, after the particles have ionized the LAr, some of the created electron-ion pairs immediately combine to produce UV scintillation light. This signal is what provides a time stamp for when the ionization was produced. This information gives the electron drift time that is used for reconstructing the position coordinates perpendicular to the anode plate. Additional orthogonal planes can be added to extend the readout to a 3-dimensional reconstruction of the events.

2.3.3   Modern and Future Experiments

Long - baseline neutrino experiments usually have three major components: the accelerator facility, the ND complex, and the Far Detector (FD) complex. The neutrinos are produced in the accelerator facility where a $\sim$ 30 GeV proton beam impinges onto a graphite target. This creates a large number of secondary hadrons that are focused through magnetic field, choosing the polarity of which allows one to choose between a neutrino or anti-neutrino enhance beam. The hadrons, mostly pions, are made to decay to muons and neutrinos along a decay volume, usually filled with helium. The muons from this are monitored to allow for beam characterization.

The neutrino beam travels a short distance and enters the ND complex. The main goal here is to characterize (monitor the flux and energy spectrum, and electron neutrino contamination) the neutrino beam before it travels further and oscillates. This complex is composed of modules of scintillator grids to also monitor beam stability and direction via the interaction of the neutrinos with the iron rich scintillators that produce charged particles detected as light.

After travelling $L \sim 10$ km, the beam arrives at the FD complex, where the number of neutrino events are counted and where the neutrino energy is reconstructed from the measured momenta of secondary particles.
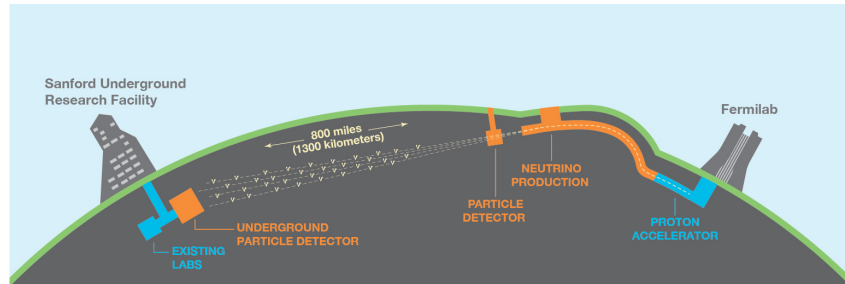
Figure 6: Overall Set-Up of the DUNE Experiment [14].

In summary, Figure 6 shows the overall set-up of the Deep Underground Neutrino Experiment (DUNE) experiment. This and the T2K experiment are two of the next generation experiments with a goal to measure the violating phase.

The NuSTEC white paper [15] outlines the future goals of the experimental and theoretical sectors of neutrino oscillation study. Among which are improvements in nuclear models, improvements in nuclear model implementation in Monte Carlo event generators, the testing of theories against accelerator-based neutrino-nucleus interaction measurements, and for current neutrino interaction programs to continue providing important data and many more.

3 Charged Current Quasielastic Scattering

3.1 Neutrino - Nucleus Cross sections

When a neutrino exchanges a neutral boson, the Z^0 boson with the target nucleon (both proton or neutron is a possible target), that is called a weak NC reaction. The product of this reaction is a neutrino of the same flavor as the original and the nucleon, as shown before in Figure 3. In a neutrino - nucleus setting, this means that the neutrino will scatter off the nucleus as a whole. However, for this thesis, the focus will be on CC interactions. This is where a charged boson, $W^{\pm}$, is exchanged with the target nucleon. At a hundred MeV to a few GeV neutrino energy, the Charged Current Quasielastic (CCQE) channel dominates the nuclear response. As shown in the same Figure 3, the CC reaction is when a neutrino interacts with a bound nucleon producing a charged lepton of the same flavor and knocks out a nucleon. In a bound nucleon setting, the CCQE-like interaction is

$$\nu_l + A \rightarrow (A - 1) + p + l, \tag{3.1}$$

$$\bar{\nu}_l + A \rightarrow (A - 1) + l^+ + n. \tag{3.2}$$

where $l = e, \mu, \tau$.

At higher neutrino energy, other charged current channels like Resonance Production (RES) where the energy transfer of the neutrino is sufficiently high to excite the nucleon into one of its resonances (Δ or N^*). The excited nucleon then decays to a nucleon and one or various mesons. For even higher energies, the Deep Inelastic Scattering (DIS) channel will dominate. Here, the incoming neutrino is energetic enough to break up the target nucleon and produce multiple particles.
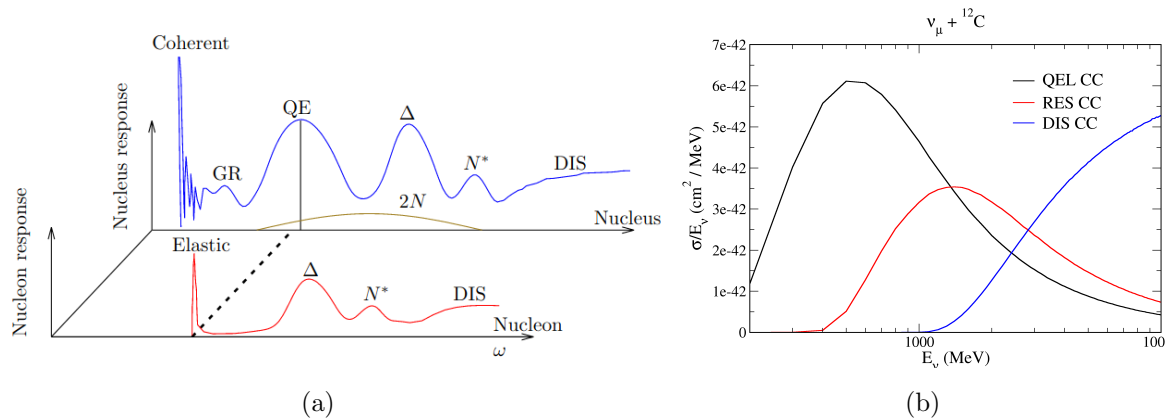
Figure 7: (a) Nuclear and nucleon responses for different reaction channels as a function of energy transfer [16]; (b) Total cross section as calculated by NuWro as a function of E_ν for different reaction channels.

The nuclear response as a function of energy transfer is shown in Figure 7a, where the dominant channels are labelled. The red curve represents the nucleon response, where the elastic channel corresponds to the a lepton scattering on an unbound nucleon. The broadening of the CCQE peak, compared to the elastic peak, is attributed to the Fermi motion of the nucleons inside a nucleus, and other nuclear effect to be discussed further in the next sections. As supplement, Figure 7b also shows the cross section values as computed in NuWro as a function of energy transfer of a muon neutrino on an oxygen target.

3.2   Elementary Cross Section Formalism

3.2.1   Variables

For the purpose of the next subsection, it will be helpful to lay out the main variables that will be used. As said, the CCQE will be the focus of this study, also more specifically the

muon neutrino will be the incoming neutrino, unless specified otherwise. These following variables will be useful to establishing the kinematics for the calculation of base neutrino - nucleon cross section without nuclear effects. The momenta of the particles involved will be denoted as

$$\text{Incoming neutrino: } K_i^\mu = (E_\nu, \vec{k}_i) \tag{3.3}$$

$$\text{Outgoing muon: } K_f^\mu = (E_f, \vec{k}_f) \tag{3.4}$$

$$\text{Initial nucleon: } P^\mu = (E, \vec{p}_m) \tag{3.5}$$

$$\text{Knockout (Final) nucleon: } P_N^\mu = (E_N, \vec{p}_N). \tag{3.6}$$
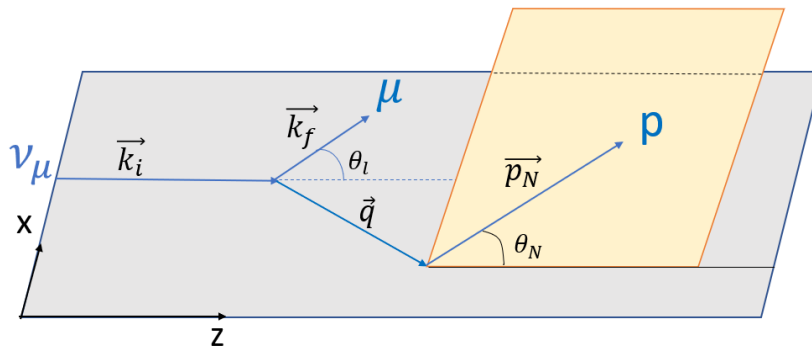
Figure 8: Diagram for the kinematics of the cross section calculation [17].

The incoming neutrino is assumed to propagate along the z-axis. This neutrino and the outgoing muon are along the xz-plane. The kinematics is shown in Figure 8, where θ_l the scattering angle of the outgoing muon with respect to the z-direction and θ_N is angle between $\vec{p}_N$ and the $\hat{z}$ direction. Furthermore, ϕ_N is defined as the proton azimuthal angle. In terms of these angles, the four momenta in the Equation 3.6 can be redefined

as

$$K_i^\mu = (E_\nu, 0, 0, k_i) \tag{3.7}$$

$$K_f^\mu = (E_f, k_f \sin\theta_l, 0, k_f \cos\theta_l) \tag{3.8}$$

$$P_N^\mu = (E_N, p_N \sin\theta_N \cos\phi_N, p_N \sin\theta_N \sin\phi_N, p_N \cos\theta_N) \tag{3.9}$$

When bound to a nucleus, the kinematics of the initial nucleon is probabilistic; however, for an unbound nucleon, P^μ could be described as plane wave solution to the free Dirac equation,

$$\Psi(X) = \sqrt{\frac{1}{2EV}} u(\vec{p}, \sigma) \exp\{(-iP \cdot X)\}, \tag{3.10}$$

where $E = \sqrt{P^2 + m_N^2}$ is the energy of the particle, V is the volume of containing the wave function, X is the four-vector length coordinate. Meanwhile, $u(\vec{p}, \sigma)$ is the four-component Dirac spinor

$$u(\vec{p}, \sigma) = \sqrt{E + M} \begin{pmatrix} \chi_s \\ \frac{\vec{\sigma} \cdot \vec{p}}{E+M} \chi_s \end{pmatrix}, \tag{3.11}$$

where M is the particle mass, $\vec{p}$ is the wave's three-momentum vector, and σ is the three-component spin projector. χ_s denotes the two-component spin state

$$\chi_{+1/2} = \begin{pmatrix} 1 \\ 0 \end{pmatrix}; \text{ and, } \chi_{-1/2} = \begin{pmatrix} 0 \\ 1 \end{pmatrix}. \tag{3.12}$$

Important note is that this Dirac spinor is normalized as $u^\dagger(\vec{p}, \sigma) u(\vec{p}, \sigma) = 2E$.

3.2.2   Cross section calculation

For a scattering of two, on-shell, Dirac particles, in this case the neutrino and the neutron, the differential cross section is calculated through

$$d^6\sigma = (2\pi)^4 \delta^4(P_N + K_f - P - K_i) \frac{1}{4E_\nu E v_{rel}} |\mathcal{M}|^2 \frac{d^3\vec{p}_N}{(2\pi)^3 2E_N} \frac{d^3\vec{k}_f}{(2\pi)^3 2e_f} \tag{3.13}$$

22

where v_{rel} is the relative speed between the velocity of the incoming neutrino and initial nucleon and $|\mathcal{M}|^2$ is the squared scattering amplitude averaged over all initial and final states. This equation only holds for collinear collisions. A more general expression is [18]

$$d^6\sigma = (2\pi)^4\delta^4(P_N + K_f - P - K_i)\frac{1}{4\sqrt{(K_i \cdot P)^2 - m_\nu^2 m_N^2}}|\mathcal{M}|^2 \times \frac{d^3\vec{p}_N}{(2\pi)^3 2E_N}\frac{d^3\vec{k}_f}{(2\pi)^3 2e_f}, \tag{3.14}$$

where the difference from Equation 3.13 and is that the flux factor is Lorentz invariant. To further simplify this, the mass of the neutrino can be neglected, $m_\nu \approx 0$.

3.2.3 Semi Inclusive Cross section

A semi-inclusive event is where the final-state particles from the interaction are also detected, in addition to the scattered lepton. From Equation 3.14, the semi inclusive cross section can be

$$\frac{d^6\sigma}{dk_f d\Omega_f dp_N d\Omega_N} = \frac{1}{(2\pi)^2}\delta^4(P_N + K_f - P - K_i)\frac{p_N^2 k_f^2}{16|K_i \cdot P|E_N e_f}|\mathcal{M}|^2. \tag{3.15}$$

Here, the momentum space volume element is expressed as $d^3p_f = k_f^2 dk_f d\Omega_f$, where $d\Omega_f = \sin\theta_f d\theta_f d\phi_f$ is the infinitessimal solid angle. Meanwhile, The squared scattering amplitude in Equation 3.15 can be broken down into the leptonic tensor, $L_{\alpha\beta}$, and the hadronic tensor, $H_{\alpha\beta}$, as

$$|\mathcal{M}|^2 = \frac{g^4\cos^2\theta_c}{M_W^4}L_{\alpha\beta}H^{\alpha\beta} \tag{3.16}$$

$$= \frac{G_F^2\cos^2\theta_c}{2}L_{\alpha\beta}H^{\alpha\beta} \tag{3.17}$$

where $\frac{g^2}{M_W^2} = \frac{G_F}{\sqrt{2}}$, and G_F is Fermi coupling constant, $G_F \approx 1.17 \times 10^{-5}\text{GeV}^2$, and $\cos\theta_c$ is the cosine of the Cabibbo quark mixing angle, $\cos\theta_c \approx 0.974$. In Equation 3.15, the

leptonic tensor can be written as

$$L_{\alpha\beta} = \sum_{s_i,s_f} \bar{u}(K_f, s_f)\gamma_\alpha(1 - \gamma_5)u(K, s_i)[\bar{u}(K_f, s_f)\gamma_\beta(1 - \gamma_5)u(K_i, s_i)]^\dagger \qquad (3.18)$$

$$= Tr[(K_i + m_\nu)\gamma_\alpha(1 - \gamma_5)(K_f + m_\mu)\gamma_\beta(1 + \gamma_5)] \qquad (3.19)$$

$$= 8[K_{i\alpha}K_{f\beta} + K_{i\beta}K_{f\alpha} - (K_i \cdot K_f)g_{\alpha\beta} - i\epsilon_{\alpha\beta\rho\sigma}K_i^\rho K_f^\sigma] \qquad (3.20)$$

$$= 8\eta_{\alpha\beta}. \qquad (3.21)$$

Meanwhile, the hadronic tensor is defined as

$$H^{\alpha\beta} = \frac{1}{2}\sum_{\sigma_i,\sigma_f} \bar{u}(P_N, \sigma_f)\Gamma_N^\alpha u(P, \sigma)[\bar{u}(P_N, \sigma_f)\Gamma_N^\beta u(P, \sigma)]^\dagger, \qquad (3.22)$$

The current operator of the nucleon, Γ_N^μ, is composed of vector and axial vector currents associated to the corresponding structures of the nucleon. It is expressed as

$$\Gamma_N^\mu = F_1^V\gamma^\mu + i\frac{F_2^2}{2m_N}\sigma^{\mu\nu}Q_\nu + G_A\gamma^\mu\gamma^5 + F_P Q^\mu\gamma^5, \qquad (3.23)$$

where

$$\sigma^{\mu\nu} = \frac{i}{2}[\gamma^\mu, \gamma^\nu]. \qquad (3.24)$$

The F_1^V and F_2^V are the form factors related to the vector component of the hadronic current, while G_A is the axial vector part and F_P is the pseudoscalar part. If the initial and final nucleons are free (unbound) and on - shell, then

$$\bar{u}(P_N, \sigma)(\gamma_\mu P_N^\mu - m_N) = 0 \qquad (3.25)$$

$$(\gamma_\mu P^\mu - m_N)u(P, \sigma) = 0. \qquad (3.26)$$

It can then be shown that Equation 3.24 can be rewritten as

$$\Gamma_N^\mu = (F_1^V + F_2^V)\gamma^\mu - F_2^V\frac{(P + P_N)^\mu}{2m_N} + G_A\gamma^\mu\gamma^5 + F_P Q^\mu\gamma^5 \qquad (3.27)$$

Substitute this to Equation 3.22 to get

$$H^{\alpha\beta} = 4m_N^2 \left(-W_1(Q^2)g^{\alpha\beta} + W_2(Q^2)\frac{P^\alpha P^\beta}{m_2^2} + iW_3(Q^2)\varepsilon^{\alpha\beta\mu\nu}\frac{P_\mu Q_\nu}{2m_N^2} \right.$$
$$\left. + W_4(Q^2)\frac{Q^\alpha Q^\beta}{m_N^2} + W_5(Q^2)\frac{P^\alpha Q^\beta + P^\beta Q^\alpha}{2m_N^2} \right). \tag{3.28}$$

$$= 4m_N^2 W^{\alpha\beta} \tag{3.29}$$

where the five structure functions, $W_i(Q^2)$, in terms of the form factors and $Q^2 = \omega^2 - q^2$, are

$$W_1(Q^2) = \frac{-Q^2}{4m_N^2}[(F_1^V + F_2^V)^2 + G_A^2] + G_A^2, \tag{3.30}$$

$$W_2(Q^2) = (F_1^V)^2 + \frac{-Q^2}{4m_N^2}(F_2^V)^2 + G_A^2, \tag{3.31}$$

$$W_3(Q^2) = 2G_A(F_1^V + F_2^V), \tag{3.32}$$

$$W_4(Q^2) = \frac{(F_2^V)^2}{4m_N^2}\left(\frac{-Q^2}{4} - m_N^2\right) - \frac{F_1^V F_2^V}{2} - F_P G_A m_N - \frac{Q^2}{4}F_P^2, \text{ and} \tag{3.33}$$

$$W_5(Q^2) = W_2(Q^2). \tag{3.34}$$

Finally, the definition of the squared scattering amplitude can be expressed as

$$|\mathcal{M}|^2 = 16G_F^2\cos^2\theta_c m_N^2 \eta_{\alpha\beta}W^{\alpha\beta}, \tag{3.35}$$

and, additionally, the cross section in Equation 3.14 for a semi-inclusive event is then

$$\frac{d^6\sigma}{dk_f d\Omega_f dp_N d\Omega_N} = \delta^4(P_N + K_f - P - K_i)\frac{G_F^2\cos^2\theta_c}{(2\pi)^2}\frac{m_N^2 p_N^2 k_f^2}{|K_i \cdot P|E_N e_f}\eta_{\alpha\beta}W^{\alpha\beta}. \tag{3.36}$$

Equation 3.36 could, therefore, be integrated over all possible $\vec{p}_N$ values to get

$$\frac{d^3\sigma}{dk_f d\Omega_f} = \delta(E_N + E_f - E - E_\nu)\frac{G_F^2\cos^2\theta_c}{(2\pi)^2}\frac{m_N^2 k_f^2}{|K_i \cdot P|E_N E_f}\eta_{\alpha\beta}W^{\alpha\beta}. \tag{3.37}$$

In terms of the muon energy E_f, the Jacobian $E_f dE_f = k_f dk_f$ can be used to redefine the inclusive cross section in Equation 3.36 to get

$$\frac{d^3\sigma}{de_f d\Omega_f} = \delta(E_N + E_f - E - E_\nu)\frac{G_F^2\cos^2\theta_c}{(2\pi)^2}\frac{m_N^2 k_f}{|K_i \cdot P|E_N}\eta_{\alpha\beta}W^{\alpha\beta}, \tag{3.38}$$

that is valid for any momentum of the initial nucleon, P^μ.

3.2.4 Setting Kinematics

If the target neutron is at rest, $P^\mu = (m_N, 0)$, by momentum conservation, the three-momentum of the knockout nucleon is now

$$\vec{p}_N = \vec{q} = \vec{k}_i - \vec{k}_f, \tag{3.39}$$

where the magnitude squared of which is

$$p_N^2 = k_i^2 + k_f^2 + 2k_i k_f \cos\theta_l \tag{3.40}$$

$$= E_\nu^2 + k_f^2 - 2E_\nu k_f \cos\theta_f, \tag{3.41}$$

where recall that θ_f is the scattering angle of the muon, μ^-, with respect to the initial direction of the neutrino, ν_μ, that is along the z-axis. In the second step, the $k_i^2 = E_\nu^2$ because of the assumption that the neutrino is massless. Using the on-shell condition on the p_N^2 in Equation 3.41, the energy of the knockout nucleon is now

$$E_N = (m_N^2 + E_\nu^2 + k_f^2 - 2E_\nu k_f \cos\theta_f)^{1/2}. \tag{3.42}$$

Substituting this into the conservation law inside the δ function in Equation 3.36, also using the on-shell condition for the muon energy, gets

$$g(k_f) = ((k_f)^{1/2} + m_f^2)^{1/2} + (m_N^2 + E_\nu^2 + k_f^2 - 2E_\nu k_f \cos\theta_f)^{1/2} - E_\nu - m_N, \tag{3.43}$$

where $g(k_f) = E_N + E_f - E - E_\nu$. The derivative of this function, in terms of k_f, is

$$\left| \frac{\partial g(k_f)}{\partial k_f} \right| = \left| \frac{k_f}{E_f} + \frac{k_f - E_\nu \cos\theta_l}{E_N} \right| \tag{3.44}$$

$$= \left| \frac{k_f(E_\nu + m_N) - E_f E_\nu \cos\theta_l}{E_f E_N} \right|, \tag{3.45}$$

where the third line is obtained using $E_N + E_f = E_\nu + m_N$.

Finally, using Equations 3.41-3.45, Equation 3.37 is integrated over the muon momentum, k_f, and the outgoing lepton azimuthal angle, ϕ_f, to get the single differential cross section

$$\frac{d\sigma}{d\cos\theta_f} = \frac{1}{|k_f(E_\nu + m_N) - E_f E_\nu \cos\theta_f|} \frac{G_F^2 \cos^2\theta_c}{2\pi} \frac{m_N k_f^2}{E_\nu} \eta_{\alpha\beta} W^{\alpha\beta}. \tag{3.46}$$

3.3   Nuclear Models

Previously, the cross section calculation are described for a neutrino, or any lepton, colliding with an unbound nucleon. In experiments, however, neutrinos are impinging on a target with nucleons that are bound to the nucleus; therefore, nuclear effects should be introduced to the CCQE vertex. In a neutrino - nucleus interaction, the coupling between the incoming lepton and nucleus can not be ignored. In the Impulse Approximation (IA), the interactions between the nucleons in the nucleus are ignored during the collision. Essentially, IA assumes that the dominant process is elastic scattering from individual nucleons in the nucleus' ground state. Here, the current that describes the coupling of the boson with the nucleus is approximately the incoherent sum of one-body currents.

For the neutrino - nucleus, at the few - GeV range where the CCQE channel is dominant, the typical values of momentum transfer is large enough to rely on the IA. In the IA, the nucleus is viewed as composed of quasi-free nucleons and that each reaction occurs on one of them. This approximation works well for $q \geq 400\text{MeV}$ [19]. At momenta lower than this, more than one nucleon could be involved in the interaction. Effects like this include the meson exchange current (MEC), especially important at large q, that represent $np - nh$ excitations that are multinucleon processes. Another effect beyond the IA model are the Final State Interactions (FSI) where the nucleon produced by the CCQE reaction interacts with the residual nucleus. These effects will be discussed in the next section of this paper.

One main ingredient to obtain the CCQE cross section is the kinematics of the initial nucleon. Determining this value for a nucleon bound to a nucleus relies on nuclear models like the Relativistic Fermi Gas (RFG) and the Spectral Function (SF) approach.

3.3.1   Relativistic Fermi Gas

The simplest nuclear model is the Relativistic Fermi Gas (RFG) model. It assumes that the nucleus is a system of infinite gas of non-interacting nucleons. In this system, all levels are occupied by nucleons up to the Fermi momentum, p_F, whose values are adjusted to reproduce the width of the QE peak in inclusive electron scattering experiments. For ^{12}C, $p_F = 228$ MeV can be used [20]. For this model, the momentum density distribution is given by

$$n(p_m) = \frac{3\mathcal{N}}{4\pi p_F^3}\Theta(p_F - p_m),\tag{3.47}$$

where the $\Theta(p_F - p_m)$ is the step function that ensures that the cross section is zero if the $p_m < p_F$. It is a good time to introduce the momentum $\vec{p}_m$, called the missing momentum, that represents the momentum of the initial nucleon that is colliding with the neutrino. The density distribution is multiplied to the Lorentz-invariant form of the cross section in Equation 3.36 and integrated over $\vec{p}_m$ to get

$$\frac{d^6\sigma}{dk_f d\Omega_f dp_N d\Omega_N} = \frac{\mathcal{N}}{4\pi p_F^3}\int_0^{p_F} d^3\vec{p}_m\delta^4(P_N+K_f-P-K_i)\Theta(p_N-p_F)\Theta(p_F-p_m)\sigma_{sn},\tag{3.48}$$

where

$$\sigma_{sn} = \frac{G_F^2\cos^2\theta_c}{(2\pi)^2}\frac{m_N^2 p_N^2 k_f^2}{(K_i\cdot P)E_N E_f}\eta_{\alpha\beta}W^{\alpha\beta}.\tag{3.49}$$

The step function $\Theta(p_N - p_F)$, meanwhile, prevents the knocked out nucleon to have a momentum lower than the Fermi momentum. The pre-factor $\frac{3\mathcal{N}}{4\pi p_F^3}$ is the normalization constant

$$\frac{3\mathcal{N}}{4\pi p_F^3}\int d\vec{p}_m\Theta(p_F - p_m) = \int d\vec{p}_m n(p_m) = \mathcal{N}.\tag{3.50}$$

This also shows that the momentum density results to $\mathcal{N}$, the total number of active nucleons in the target nucleus, when integrated over $\vec{p}_m$. The integral in Equation 3.48 can be done through breaking down the δ function

$$\delta^4(P_N + K_f - P - K_i) = \delta^3(\vec{p}_N + \vec{k}_f - \vec{p}_m - \vec{k}_i)\delta(E_N + E_f - E - E_\nu)\tag{3.51}$$

to get the semi-inclusive cross section for the RFG model

$$\frac{d^6\sigma}{dk_f d\Omega_f dp_N d\Omega_N} = \frac{3\mathcal{N}}{4\pi p_F^3}\delta(E_N + E_f - E - E_\nu)\Theta(p_N - p_F)\Theta(p_F - p_m)\sigma_{sn}. \tag{3.52}$$

For a more inclusive cross section, where only the final lepton is detected, Equation 3.52 is integrated over p_N. To do this, the δ must first be expressed as a function of the independent variables $\vec{k}_i$, $\vec{k}_f$, and $\vec{p}_N$

$$f(p_N) = E_f + E_N - E - E_\nu \tag{3.53}$$

$$= \sqrt{p_N^2 + m_N^2} - \sqrt{p_N^2 + q^2 - 2p_N q \cos\theta_{Nq} + m_N^2} - \omega, \tag{3.54}$$

where θ_{Nq} is the angle between $\vec{p}_N$ and the three-momentum transfer, $\vec{q}$. The expression $f(p_N)$ should be zero giving the solution

$$p_N^\pm = \frac{AB \pm \sqrt{A^2 + (B^2 - 1)^2 m_N^2}}{B^2 - 1}, \tag{3.55}$$

where

$$A \equiv \frac{|Q^2|}{2\omega} \tag{3.56}$$

$$B \equiv \frac{q\cos\theta_{Nq}}{\omega}. \tag{3.57}$$

There are two possible solutions for p_N: p_N^+ and p_N^-. Meaning, that for a certain configuration of $\vec{k}_i$, $\vec{k}_f$, and $\vec{p}_N$, there are two final nucleon momentum values that satisfy the conservation of energy and momentum; however, only one of these two solutions is valid, where the other one leads to a negative value of p_N. For the case where the final nucleon is not detected, the cross section will be the sum of the cross sections calculated for each p_N value

$$\delta[f(p_N)] = \frac{\delta(p_N - p_N^+)}{f_{rec}^+} + \frac{\delta(p_N - p_N^-)}{f_{rec}^-}, \tag{3.58}$$

where

$$f_{rec}^\pm \equiv \left|\frac{\partial f(p_N)}{\partial p_N}\right|_{p_N^\pm} = \left|\frac{p_N}{E_N} - \frac{p_N - q\cos\theta_{Nq}}{E}\right|_{p_N^\pm}. \tag{3.59}$$

Substituting in $\delta[f(p_n)]$ into Equation 3.52 gives

$$\frac{d^5\sigma}{dk_f d\Omega_f d\Omega_N} = \frac{3\mathcal{N}}{4\pi p_F^3} \int dp_N \Theta(p_N - p_F)\Theta(p_F - p_m)\sigma_{sn}$$
$$\times \left[\frac{\delta(p_N - p_N^+)}{f_{rec}^+} + \frac{\delta(p_N - p_N^-)}{f_{rec}^-}\right]. \tag{3.60}$$

Performing the integral gets

$$\frac{d^5\sigma}{dk_f d\Omega_f d\Omega_N} = \left(\frac{d^5\sigma}{dk_f d\Omega_f d\Omega_N}\right)_{p_N^+} + \left(\frac{d^5\sigma}{dk_f d\Omega_f d\Omega_N}\right)_{p_N^-}, \tag{3.61}$$

where

$$\left(\frac{d^5\sigma}{dk_f d\Omega_f d\Omega_N}\right)_{p_N^\pm} = \frac{3\mathcal{N}}{4\pi p_F^3}\frac{1}{f_{rec}^\pm}[\Theta(p_N - p_F)\Theta(p_F - p_m)\sigma_{sn}]_{p_N^\pm}. \tag{3.62}$$

To get the inclusive cross section, Equation 3.61 could be integrated over Ω_N through

$$\frac{d^3\sigma}{dk_f d\Omega_l} = \int d\Omega_N \left[\left(\frac{d^5\sigma}{dk_f d\Omega_f d\Omega_N}\right)_{p_N^+} + \left(\frac{d^5\sigma}{dk_f d\Omega_f d\Omega_N}\right)_{p_N^-}\right]. \tag{3.63}$$

When the neutrino flux spectra is known, the cross section can be obtained by integrating Equation 3.52 over E_ν

$$\frac{d^6\sigma}{dk_f d\Omega_f dp_N d\Omega_N} = \frac{3\mathcal{N}}{4\pi p_F^3} \int_0^\infty dE_\nu C_\nu \Phi(E_\nu)\delta(E_N + e_f - E - E_\nu)$$
$$\times \Theta(p_N - p_F)\Theta(p_F - p_m)\sigma_{sn}, \tag{3.64}$$

where $C_\nu = \left(\int_0^\infty dE_\nu \Phi(E_\nu)\right)^{-1}$ is the normalization constant. To evaluate this, it is useful to express E_ν through new variables $\vec{p}_B$, E_B and θ_B defined as

$$\vec{p}_B \equiv \vec{k}_f + \vec{p}_N = \vec{k}_i + \vec{p}_m, \tag{3.65}$$

$$E_B \equiv E_f + E_N = E_\nu + E, \tag{3.66}$$

$$\cos\theta_B \equiv \frac{\vec{k}_i \cdot \vec{p}_B}{k_i p_B} = \frac{\vec{k}_i \cdot \vec{p}_B}{E_\nu p_B}. \tag{3.67}$$

The function inside the δ: $g(E_\nu) = E_N + E_f - E - E_\nu$ can be rewritten using these variables,

$$g(E_\nu) = E_B - \sqrt{p_B^2 + E_\nu^2 - 2E_\nu p_b \cos\theta_B + m_N^2} - E_\nu. \tag{3.68}$$

Therefore the delta function becomes

$$\delta(g(E_\nu)) = \frac{E}{E_B - p_B \cos\theta_B}\delta(E_\nu - E_\nu^0),$$

(3.69)

where E_ν^0 is the solution when $g(E_\nu) = 0$,

$$E_\nu^0 = \frac{E_B^2 - p_B^2 - m_N^2}{2(E_B - p_B \cos\theta_B)}.$$

(3.70)

Equation 3.64 then becomes

$$\frac{d^6\sigma}{dk_f d\Omega_f dp_N d\Omega_N} = \frac{3\mathcal{N}}{4\pi p_F}C_\nu \Phi(E_\nu^0)\Theta(p_N - p_F)\Theta(p_F - p_m)\frac{E}{E_B - p_B \cos\theta_B}\sigma_{sn}.$$

(3.71)

Similarly, the final flux folded inclusive cross section can be computed by integrating this equation over the momentum of the knockout nucleon, p_N, and the solid angle, Ω_N,

$$\frac{d^3\sigma}{dk_f d\Omega_f} = \int d\Omega_N \int dp_N \frac{d^6\sigma}{dk_f d\Omega_f dp_N d\Omega_N}.$$

(3.72)

Interestingly, the inclusive cross sections, no flux and flux-folded, of the RFG model are possible to obtain analytically [20] and numerically. Further into this chapter, inclusive cross section plots under the RFG model calculated numerically will be presented.

3.3.2   Spectral Function Approach

Despite the simplicity of the RFG model, it is still used in many analysis and reconstructs many experimental data well. However, from electron scattering data, the interaction of the nucleon with the other nucleons of the residual system significantly affects the nucleon momentum distribution inside the nucleus. The Spectral Function (SF) is based on the shell model with short range correlation (SRC) included. This approach gives a more accurate representation of the nuclei.

The SF gives the probability distribution of removing a nucleon with the momentum $\vec{p}_m$ and leaving the residual nucleus with the excitation energy E_m. This probability

distribution can be represented by [21]

$$S(p_m, E_m)\Lambda^+(\vec{p}_m) = \sum_s \langle \Psi_A(P_A)|P, s; \Psi_{A-1}(P_{A-1})\rangle \langle P, s; \Psi_{A-1}(P_{A-1})|\Psi_A(P_A)\rangle, \quad (3.73)$$

where $\Psi_A(P_A)$ and $\Psi_{A-1}(P_{A-1})$ are wave functions of the target nucleus (A number of active nucleons) and the residual nucleus ($A-1$ number of active nucleons), respectively. $\Lambda^+(\vec{p}_m)$ is the positive energy projection operator. The recoil kinetic energy of the residual nucleus is negligible under the assumption that $p_m \ll m_{A-1}$. When the spectral function is integrated over p_m, the nucleon momentum distribution is obtained and given by

$$n(p_m) = \int_0^\infty dE_m \ S(p_m, E_m), \quad (3.74)$$

and recall that $n(p_m)$ normalized to the number of nucleons, as in Equation 3.50,

$$\mathcal{N} = C_{sf} \int d^3\vec{p}_m \int_0^\infty dE_m S(p_m, E_m). \quad (3.75)$$

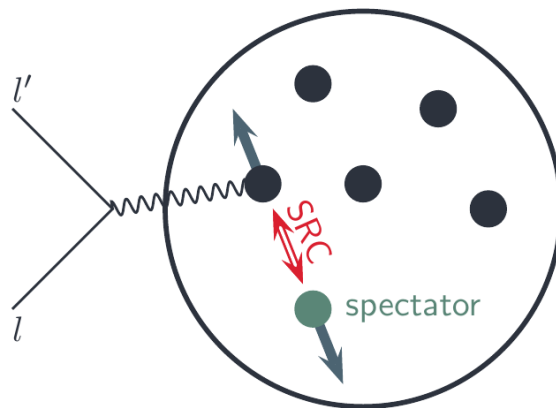where the normalization constant is found to be $C_{sf} = 0.5$ for ^{16}O [22].

Figure 9: Lepton interacts with a pair of nucleons correlated through the SRC [23].

Through the study of electron - nucleon scattering [24], i.e. (e, e'), $(e, e'p)$ and $(e, e'pN)$ scattering, it is found that around 80% of events occur where a single nucleon is moving

in a mean field potential and the rest happens on a correlated nucleon (via SRC), as shown in Figure 9. This correlation means the nucleon is paired with a spectator nucleon that is of opposite isospin and can also be knocked-out of the nucleus. Therefore the spectral function can be represented as the sum between its mean field and correlation components:

$$S(\vec{p}_m, E_m) = S_{MF}(\vec{p}_m, E_m) + S_{corr}(\vec{p}_m, E_m). \tag{3.76}$$

To calculate the inclusive cross section under the SF model, Equation 3.37 is integrated over p_m. Unlike in the RFG model, there is no step function for the restriction for the initial and final nucleon momenta. This requirement is imposed on the nucleon momentum distribution given by the SF function. The semi inclusive cross section is now

$$\frac{d^6\sigma}{dk_f d\Omega_f dp_N d\Omega_N} = \int_0^\infty dE_m \int d^3\vec{p}_m C_{sf} S(p_m, E_m) \delta^3(\vec{p}_N + \vec{k}_f - \vec{p}_m - \vec{k}_i)$$
$$\times \delta(E_\nu - E_f + m_N - E_m - E_N)\sigma_{sn}. \tag{3.77}$$

This can be integrated over p_m and E_m through the delta function that imposes that

$$E_m = \omega + m_N - E_N \tag{3.78}$$

and

$$\vec{p}_m = \vec{p}_N - \vec{q}. \tag{3.79}$$

with magnitude

$$p_m = (p_N^2 + q^2 - 2qp_N \cos\theta_{Nq})^{1/2}. \tag{3.80}$$

An inclusive cross section is obtained by further integrating over the variable for the knocked out nucleon, p_N and Ω_N,

$$\frac{d^3\sigma}{dk_f d\Omega_f} = \int dp_N \int d\Omega_N C_{sf} S(p_m, E_m)\sigma_{sn}. \tag{3.81}$$

Furthermore, for the flux-folded case, 3.77 is multiplied with C_ν, like in Equation 3.64

$$\frac{d^6\sigma}{dk_f d\Omega_f dp_N d\Omega_N} = \int_0^\infty dE_\nu^0 C_\nu \Phi(E_\nu^0) C_{sf} S(p_m, E_m)\sigma_{sn}, \tag{3.82}$$

where the zero solution of the delta function is

$$E_\nu^0 = E_f + E_N + E_m - m_N. \tag{3.83}$$

Finally, the inclusive cross section is obtained through further integration over p_N and Ω_N

$$\frac{d^3\sigma}{dk_f d\Omega_f} = \int dp_N \int d\Omega_N \int_0^\infty dE_\nu C_\nu \Phi(E_\nu) C_{sf} S(p_m, E_m) \sigma_{sn}. \tag{3.84}$$

3.4 Results and Discussion

To demonstrate the differences between the SF and RFG model, Equations 3.52 and 3.77 can be numerically solved through code. Figure (10) shows this comparison for both the no flux and flux folded case. Note that there will a change in subscripts for the outgoing lepton parameters, where $f \to \mu$ to denote that the outgoing lepton is a muon.
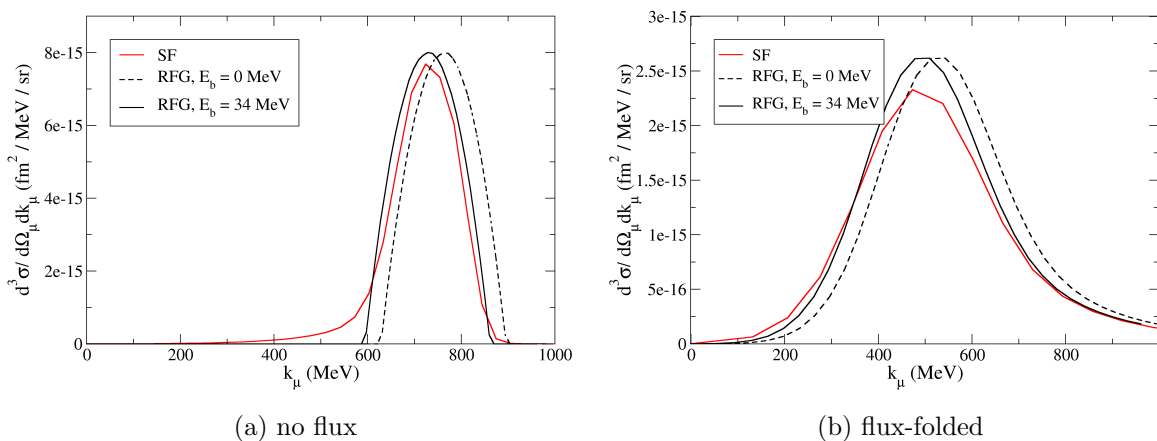

(a) no flux

(b) flux-folded

Figure 10: Inclusive cross section for both the (a) no flux case and the (b) flux-folded for the $\nu_\mu + {}^{16}O$ scattering as a function of E_ν, with kinematics $\theta_\mu = 45°$ and $k_\mu = 2000$ MeV.

This is the inclusive cross section for a muon neutrino beam of energy $E_\nu = 1000$ MeV and at lepton scattering angle of $\theta_\mu = 45°$ and $25°$. The RFG model gives a more symmetric curve because the SF model accounts for nucleon correlations, therefore

showing a low-momentum tail of the outgoing muon. The peak of RFG can be adjusted to get closer to SF, and therefore the experimental data [17] by introducing the binding energy potential. If the binding energy is introduced, the initial nucleon energy becomes

$$E = \sqrt{p_m^2 + m_N^2} - E_b, \tag{3.85}$$

where E_b is the binding energy of the target nucleus. The p_N for the RFG model can be obtained through substituting the energy transfer, ω, with $\omega' = \omega - E_b$. For oxygen, the value used is $E_b = 34$ MeV.
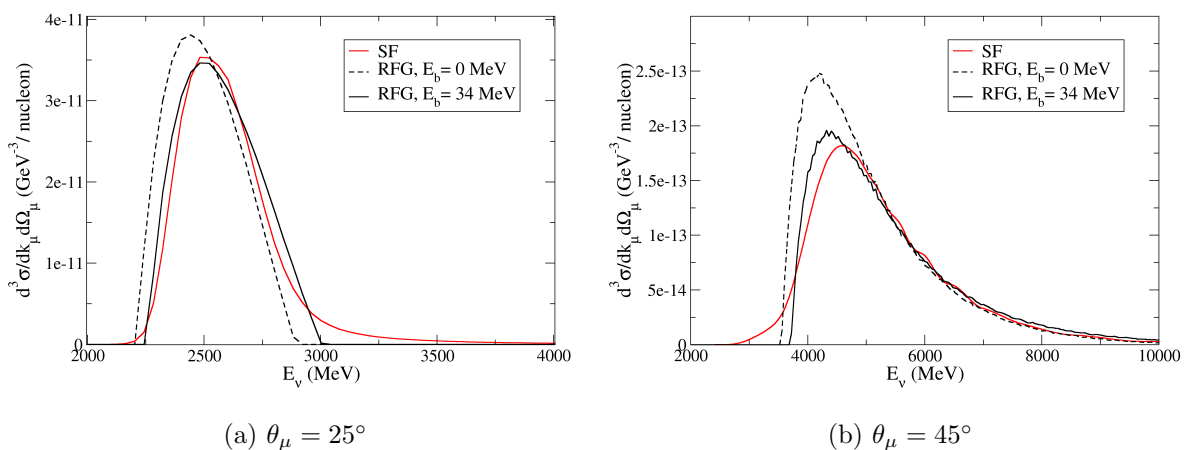

Figure 11: Inclusive cross section for the $\nu_\mu + {}^{16}O$ scattering, with kinematics $E_\nu = 1000$ MeV and (a) $\theta_\mu = 25°$ or (b) $\theta_\mu = 45°$.

The inclusive cross section can be obtained as a function of neutrino energy, E_ν. Figure 11 is the inclusive cross section for two outgoing muon kinematics of $\theta_\mu = 25°$ and $45°$, both for $k_\mu = 2000$ MeV. This is especially useful for reconstruction of the neutrino energy where the outgoing lepton kinematics is detected. The RFG model peak gets closer to that of the SF model when the binding energy is accounted for.

The RFG model is useful for when there is no interactions between the nucleons in the nucleus. Basically, the protons and nucleons are treated independently from each other as

they move in a Fermi motion inside the nucleus within the nuclear volume as dictated by the binding potential. In NuWro, the average binding energy per nucleon is represented by the *kaskada_w* parameter set at a default 7 MeV.

NuWro provides the option to implement the RFG models in two ways, locally (LFG) and globally (FG). *Globally* meant that the nucleus is treated as a perfect sphere of radius $R = r_0 A^{1/3}$, where $r_0 = 1.25 \pm 0.20$ fm and A is the atomic mass number, with constant nuclear density $\rho = A(\frac{4}{3}\pi R^3)^{1/3}$. This also meant that the nuclear binding potential and the Fermi level are constant all throughout the nucleus.

Alternatively, the nucleus can be described in the FG picture using the local density approximation (LDA) [25, 26] where the nuclear density can be described through a distribution, $\rho(r)$, obtained from data from electron scattering experiments [27]. This Fermi momentum is not constant and is dependent on ρ in the following way

$$p_F^{(p)}(r) = \hbar\left(3\pi^2\rho(r)\frac{Z}{A}\right)^{1/3} \tag{3.86}$$

$$p_F^{(n)}(r) = \hbar\left(3\pi^2\rho(r)\frac{A-Z}{A}\right)^{1/3}. \tag{3.87}$$

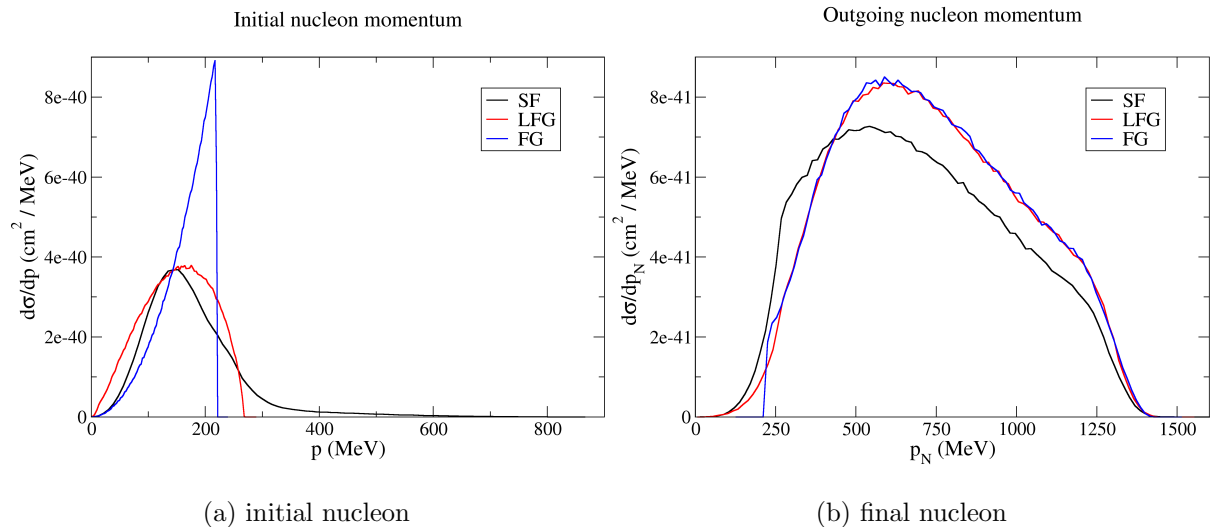(a) initial nucleon   (b) final nucleon

Figure 12: Comparison of momentum spectra for the SF, LFG, and FG for the (a) initial nucleon and (b) knocked-out nucleon.

Figure 12 shows the initial nucleon momentum for the three models, SF and Global Fermi Gas (FG) and Local Fermi Gas (LFG) as obtained through NuWro. There is an unnatural cut for the FG momenta distribution for values above p_F. When LDA is introduced through the LFG model, this distribution comes closer to that of the SF. The difference between LFG and SF, is that SF features a high-momentum tail due to the contribution of the nucleon correlation component of the SF, as seen in Equation 3.76. To the right of Figure 12 is the final knockout nucleon momentum distribution of each model, where the unphysical cut in FG is evident, limiting final nucleons to have a momentum lower than p_F, which is the consequence of Pauli Blocking (PB) effect. The PB effect forbids fermions to be in the same quantum state but in the SF approach, not all states up to Fermi level are occupied. Meanwhile, the PB effect still manifests in the LFG and SF model through the fact that there are less events in the lower momentum range, there is no unphysical cut because the p_F for these models occur in a distribution.

Details on NuWro will be discussed in more detail in the next chapter. However, for

37

the purposes of the current discussion, it is important to note that in NuWro, each event is generated with a probability proportional to the cross section. The differential cross section per nucleon over some parameter x can be obtained from the event histogram via

$$\left. \frac{d\sigma}{dx} \right|_{x=x_0} \rightarrow \frac{N(x = x_0 \pm \Delta x/2)}{N_{total}} \frac{\sigma_{total}}{\Delta x}, \tag{3.88}$$

where $N(x = x_0 \pm \Delta x/2)$ is the event count for x value centered at x_0 over a bin width of Δx. σ_{total} is the total cross section per nucleon for a certain reaction channel and N_{total} is the total number of events for this particular reaction channel. Consequently, for i^{th} order differential cross sections

$$\frac{d\sigma}{dx_1 dx_2 ... dx_i} \rightarrow \frac{N(x = x_{0,1} \pm \Delta x_1/2, ..., x_i = x_{0,i} \pm \Delta x_i/2)}{N_{total}} \frac{\sigma_{total}}{\Delta x_1 \Delta x_2 ... \Delta x_i}. \tag{3.89}$$

As previously stated, the leptonic and hadronic tensors can be solved numerically to calculate the inclusive cross section. This calculation can be compared to that of NuWro for different models. Figure 13 shows this comparison for a muon neutrino beam of energy 750 MeV. It can be seen that the NuWro SF simulates high-ω tail well, when compared to the numerical calculation os SF. Of the NuWro calculations, it is the SF model that gave the plot that is closest to magnitude of the numerically-obtained cross sections.
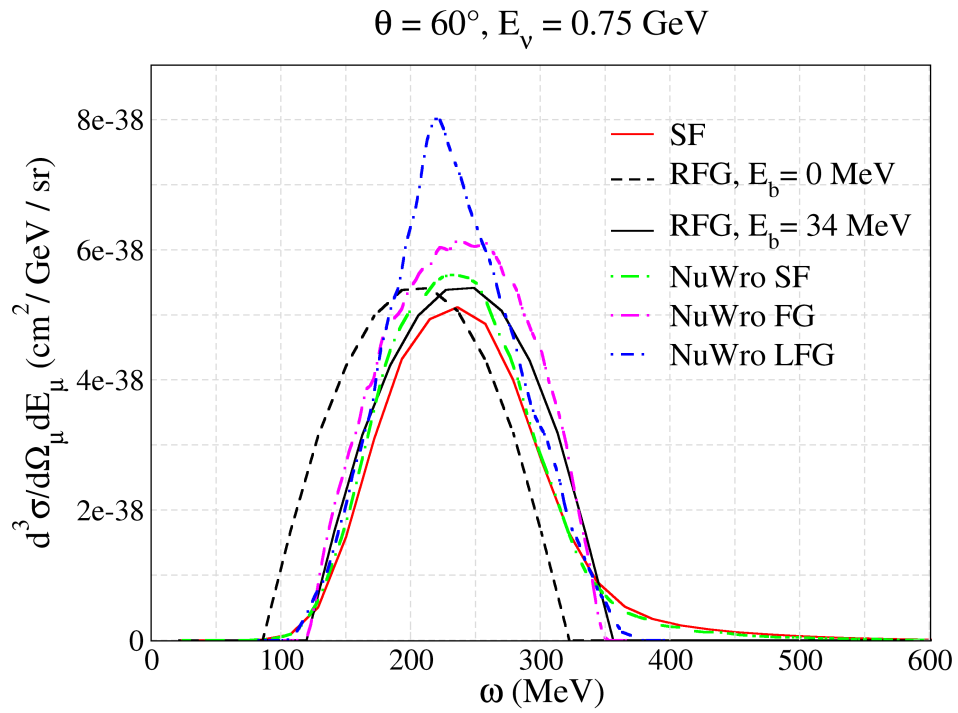
Figure 13: Double differential cross section for different nuclear models compared to NuWro calculation for the $\nu_\mu + {}^{16}O$. This is for the no flux case.

4   NuWro Analyses

4.1   Monte Carlo Event Generators and NuWro

Electron scattering on nuclei has been an active field over a long time. It has been very helpful on obtaining knowledge about the nucleus' electromagnetic interactions, for different ranges of energies. It enabled physicists to study nuclear phenomena like final state interactions. If these studies are to be extended to the nucleus' reaction with neutrinos, there are new degrees of freedom arising from the weak interaction to explore. Both electron-induced and neutrino-induced reaction studies are very similar to each other but features very fundamental differences. In the electron-induced reaction, the incoming electron beam energy is very accurately known, whose momenta can be measured through magnetic spectrometers. But like described earlier, neutrinos are produced through a secondary decay of pions and kaons, so their energies are smeared over a range of values. To extract the oscillation parameters, the incoming neutrino energy is required. This energy is therefore reconstructed through the measurement of the final state of the neutrino-nucleus reaction. This reconstruction involves a wide extrapolation of the measured (detected) final state to the actual and full final state.

There are two methods used to reconstruct the neutrino energy from the final state particles. One is the kinematical method, where the incoming neutrino energy can be determined by the kinematics of the outgoing lepton. There are complications to this methods especially when the nuclear effects in the target are not accounted for. This problem is addressed by the second method, the calorimetric method. This method is where the energies of all outgoing particles in the final state is measured and the energy of the neutrino is reconstructed from that information. This method relies on the detectors being able to detect all the outgoing particles, which is not realistic.

In both of these methods, a neutrino energy value is reconstructed from the measured

40

final state, whether from the outgoing leptons or from all the particle the detector could find. This *measured* energy should be extrapolated to the *true* energy. This is where the role of neutrino event generators comes in.

Basically, Monte Carlo neutrino generators are codes or libraries of cross section data that not only simulate final neutrino-nucleon, -electron, and -nuclei interactions, but also the important final state interactions. Their usual task is to take a neutrino and nucleus as input and give a set of 4-vectors for particles emerging from the interaction, from the channel vertex and from the re-interactions with the residual nucleus. This information is essential to full detector simulations. Besides their role in energy reconstruction, these generators are critical to the convolution of the flux of the neutrino beam, neutrino interaction physics, and detector response that is needed to make predictions on observable quantities. Currently, there are several neutrino event generators available, some examples are GENIE [28] , GIBUU [29, 30], NEUT [31], and NuWro. The NEUT generator is mainly used in the T2K experiment, the GENIE generator is widely used in Fermilab experiments. Lastly, the focus of this study, NuWro, that is being used for comparing theory and experimental results.

The NuWro MC generator [23, 32–34] is developed by theorists of the Wroclaw University since 2005. The basic motivation was "to develop a tool to understand the impact of various theoretical approaches to neutrino interactions on observables". This generator simulates neutrino-nucleon and -nucleus interactions for neutrino energies ranging from ~ 100 MeV to ~ 100 GeV. It implements the nuclear models discussed in this paper, the Spectral Function and two versions of the Fermi Gas model, along with other options. NuWro has four dynamical models: Charged Current Quasielastic (CCQE) reaction (Elastic for the NC version), Resonance Production (RES), Deep Inelastic Scattering (DIS), and the coherent pion production. These channels can be switched on or off for a simulation, in this thesis's case, only the CCQE channel will be turned on, unless indicated otherwise. NuWro's modelling of the Final State Interactions (FSI) was introduced into

the code by C. Juszczak and team [33].

The code for NuWro is written in C++ language. A simulation's input file contains parameters like: nuclear model options, dynamics channel options, form factors sets, neutrino beam composition and energies, target specifications, and final state interaction parameters and the cascade model parameters. The output files have flux-averaged cross section values in *.txt* files and different event spectra in a *.root* file. This root file is analyzed using the NuWro-adapted *myroot* application.

4.2 Final State Interactions

When a proton is produced through CCQE interaction of a neutrino and a bound neutron, it doesn't escape the nucleus so easily. Instead it can re-interact with other nucleons in the residual system. This additional interaction can either produce pions or knock out more nucleons. Figure 14 shows the possible re-interactions of a proton produced by a CCQE vertex. As shown, the possible final state interaction channels are the elastic nucleon-nucleon interaction, nucleon single pion production and double pion production, and nucleon charge exchange. The new pions produced can also interact with the residual system elastically and inelastically.

One of the first attempts of modelling the trajectory of hadrons in nuclear matter was through the Monte Carlo approach implemented by Metropolis [35]. This model is the IntraNuclear Cascade (INC). Cascade models are based on theoretical assumptions that limit their applicability. This is of great importance on the analyses on FSIs of nucleons from the CCQE vertex that will travel through the nucleus. Characterizing the effect of FSI on the momentum of the final state protons is essential to reducing systematic errors in the experiments. Of the four event generators used in neutrino experiments, NEUT, GENIE, NuWro, and GIBUU, the first three use the INC in modelling FSI. In NuWro, the implementation of this cascade model is regularly updated with the inclusion of the Oset

model [36, 37] of effective pion-nucleon (piN) cross sections and other upgrades like models for multi-pion production cross sections in pion-nucleon interactions and implementation of angular distributions in the pion-nucleon scattering. Ultimately, calculations through this model should recreate nuclear transparency data [38].
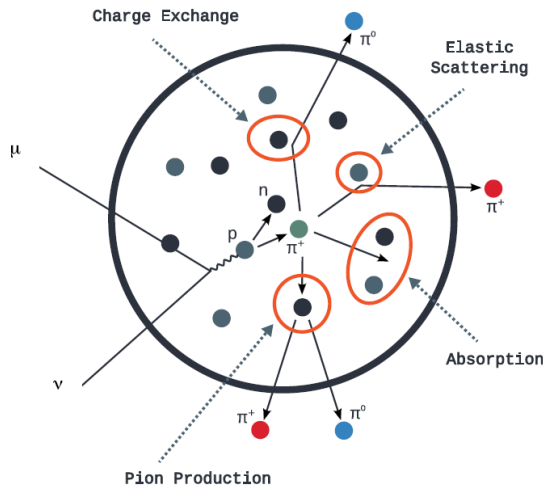

Figure 14: Final State Interactions for a scattered proton [23].

Nuclear transparency is defined as the probability that a knocked out nucleon will not be subjected to interactions with components of the residual nucleus. This is extensively studied using electron - proton scattering experiments on different nuclei. The focus of this thesis, NuWro, was found to describe nuclear transparency data *very well* [39]. How NuWro samples for the INC is based on the standard probability of a particle to propagate over a distance Δx with no re-interactions:

$$P(\Delta x) = \exp(-\Delta x/\lambda), \tag{4.1}$$

where λ is the mean free path expressed in terms of the local nuclear density ρ and an effective pion or nucleon interaction cross section. The nucleons or pions produced in the reaction vertex to be subjected to FSI are put in a queue, where the mean free path

defined by Equation 4.1 is calculated according to the particle's position. This mean free path is subjected to selection rules that determine whether this particle can be listed as an outgoing particle, a particle that interacts with the residual system, or is absorbed by the nuclear matter. If this particle is determined to interact with the medium, an interaction type is selected and the kinematics is generated by NuWro.

Figure 15 shows the block diagram of how NuWro generates a nucleon interaction inside the FSI. The probability of generating a nucleon interaction to either be elastic interaction, single pion production and double pion production, is described by f_{inel} and f_{π} parameters as defined by the piN and nucleon-nucleon (NN) models implemented in NuWro. After generating this interaction, PB is checked. If interaction is Pauli-blocked, the particle is reinserted back to the queue. Because NuWro is able to separate the information about the secondary particles before and after being subjected to FSI, a study of the effects of the FSI on the proton entering the cascade can be done. The momentum spectra of different configurations of the final state could then be compared to theoretical computations.
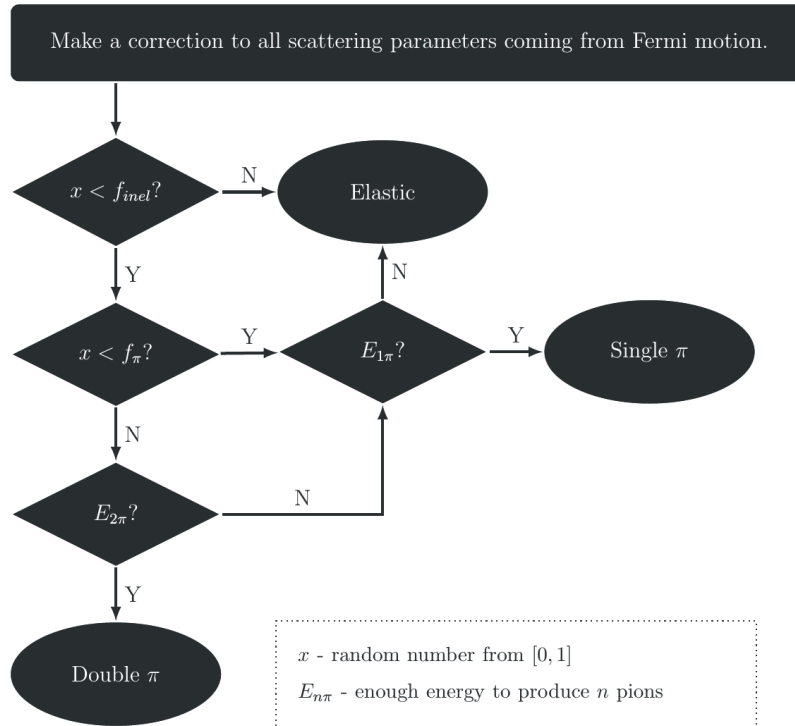
Figure 15: Diagram of NuWro for generating nucleon-nucleon interaction events [23]

For clarity, it is important to note that the cascade model is different from the nuclear models like SF or LFG. The SF and LFG describe the initial state and dynamics of the bound nucleon as it interacts with the neutrino. Meanwhile, the cascade model describes the propagation of the nucleon/s, the products of the CCQE vertex, through the residual system.

4.3   Results and Discussion

4.3.1   Different Final States

Equation 3.89 establishes that the probability that generators generate an event is dependent to the channel cross section. Event histograms are stored in ROOT as trees

and can be accessed through the TTree::Draw function. These histograms can be filtered according to parameter values. A cut can be set so that a spectrum only has events of a particular final state. A final-state nucleon is essentially the nucleon being detected, therefore FSI has to be taken into account. Whether the lepton is also detected or not is not relevant in the following discussions.
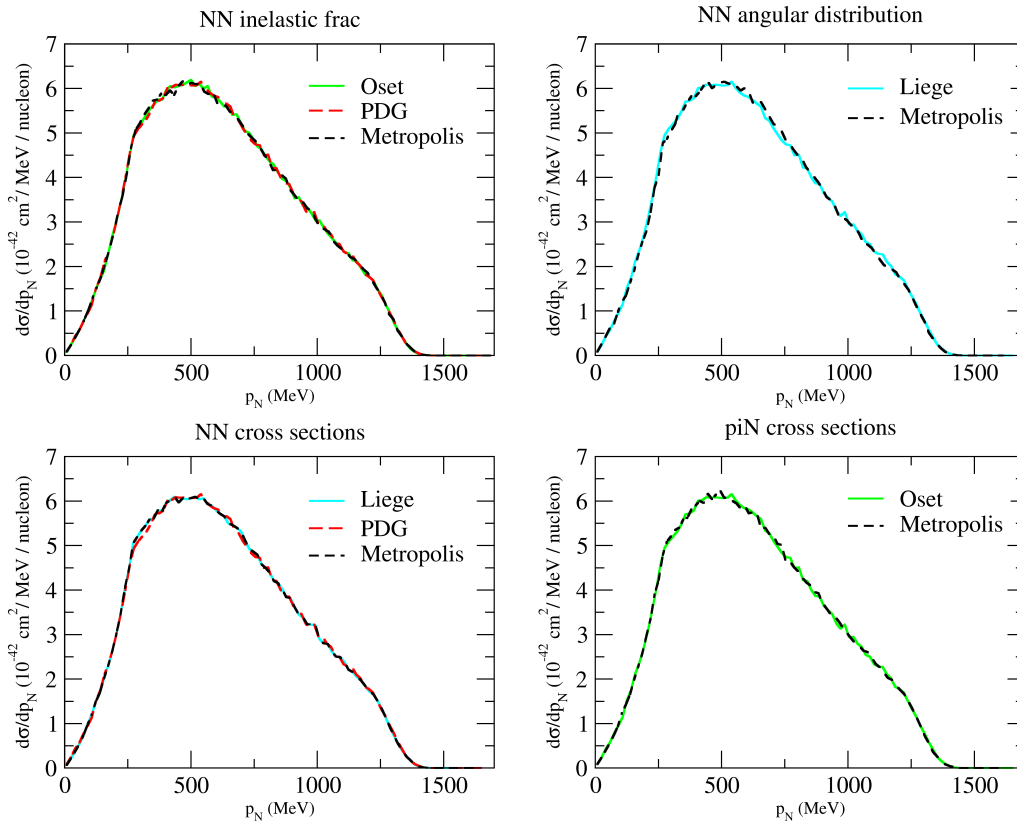

Figure 16: Comparison of different NN and piN interaction models.

For the purposes of the following discussion, the notation "ip $j\pi$ kn" is used to denote a final state where there is i protons, j pions, and k neutrons escaping the nucleus after the cascade. Additionally, when a signal is labelled as $1p$, it means there is 1 proton exiting the nucleus but it can also include events where there are accompanying pions

and neutrons. Also, a signal is labelled as $1p\_atleast$ when there is more than 1 proton knocked out of the nucleus. For the following figures, this spectra is usually presented as a function of the momentum of the leading proton, the final-state nucleon. The leading proton is the proton that has the highest momentum among all the protons exiting the nucleus and detected in experiments. This leading proton is mostly also the leading nucleon, however there are states where the proton is either absorbed by the nucleus or the exiting neutron has higher energy than the proton. The parameter p_N used in this chapter is the momentum of this leading proton.

The NN and piN cross sections from different models (Metropolis [35], Oset [36, 37], PDG2016 [40], Liege [41]) implemented in NuWro can be compared to each other but it is shown to not have much effect on relevant curves, as shown in Figure 16. From here on, the NuWro settings for the NN and piN cross sections are set to the default.

Figure 17 shows the single differential cross section for $1p$, $2p$ and $3p$ for neutrino energies 500, 1000, and 2000 MeV. For reference, the most general case that is the $1p\_atleast$ signal is also presented. Figure 18a shows when the single differential cross sections in Figure 17 are integrated over the outgoing nucleon momentum, p_N. Figure 18b plots the $1p$, $2p$, and $3p$ spectra as a fraction of the sum $1p\_atleast$ signal. These fractions approaches constant values, with the $1p$ channel dominant in all energies, covering 70% of the total number of events.

Figure 19 and 20 breaks down the $1p$ and $2p$ final state, respectively, into its $0n$, $1n$, $2n$ components. The $0n$ is dominant, say, covering a total of 80% of $1p$ events for $E_\nu = 1000$ MeV in the $1p$ state. However, at lower momenta, the $1n$ and $2n$ cross sections could have higher values. The knocking out of a neutron is a result of inelastic scattering, either by the proton charge exchange and pion production, in the FSI.
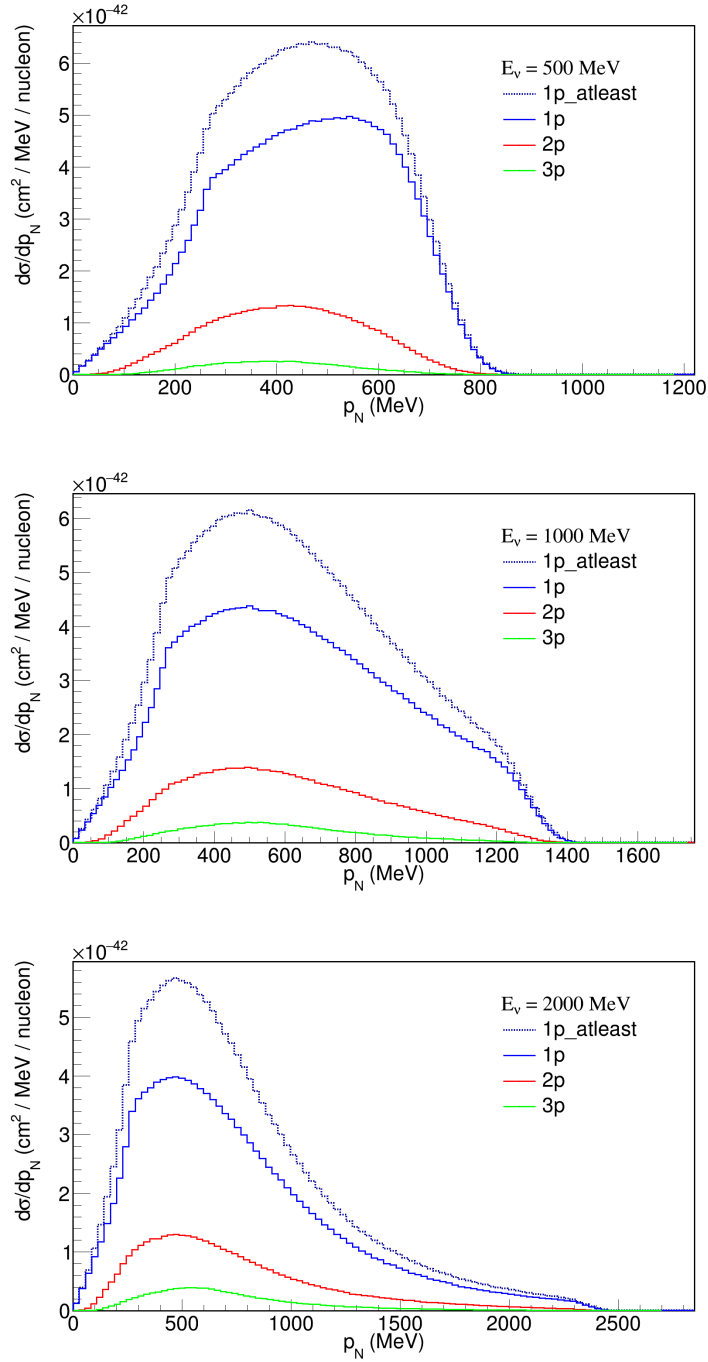
Figure 17: Single differential cross section for the breakdown of the 1p_atleast final state into the 1p, 2p, and 3p final states for different neutrino energy values: (top to bottom) $E_\nu = 500, 1000,$ and 2000 MeV.
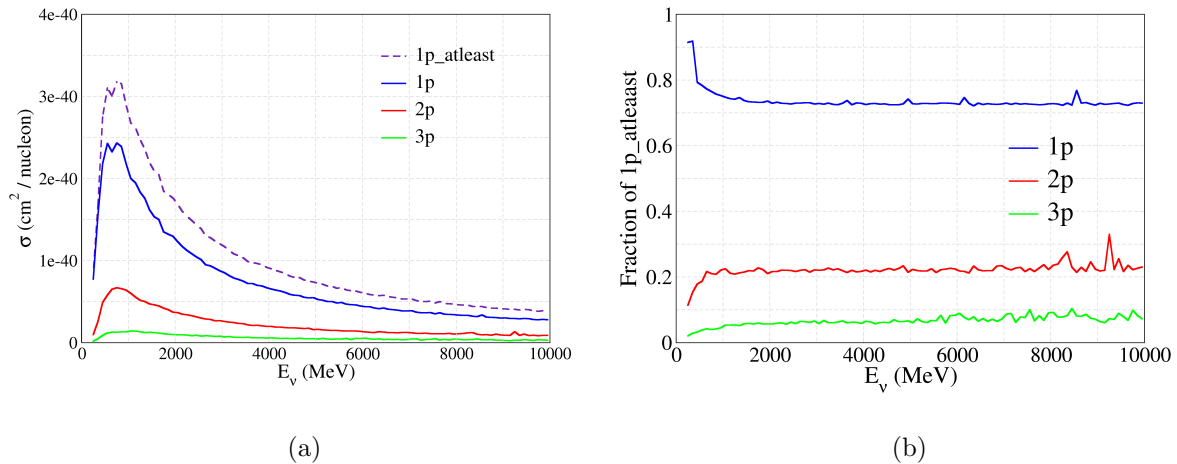
48

Figure 18: (a) Total cross section as a function of neutrino energy for final states $1p\_atleast$, $1p, 2p$, and $3p$. (b) Fraction of the $1p\_atleast$ that is the $1p$, $2p$, and $3p$ final state.

In the CCQE case, pions are only produced through the FSI. Possible pion channels in the FSI are elastic scattering, charge exchange, and single and double pion production, and also absorption (absorbed by the nucleus). The pion production interaction can also be observed through Figure 21. The 0π signals are dominant and has cross sections that is magnitudes higher that the multi-pion signals, with 1π much more likely than 2π. The 1π and 2π curves combined cover only 1.3% of the $1p$ events (for $E_\nu = 1000$).

Furthermore, pions exiting the nucleus could either be π^0, π^+, or π^-. Figure 22a and 22b examines the $1p1\pi$ cross section as a function of the proton momentum and the pion momentum, respectively. Based on these figures, the π^+ is most likely to be produced and knocked out of the nucleus. Furthermore, pions knocked out of the nucleus occupy low momentum values. It can be said that these pions are also produced with low momentum values which explains the low probability of 1π and 2π final states because these pions are absorbed by the nucleus when their energy is below the binding energy.
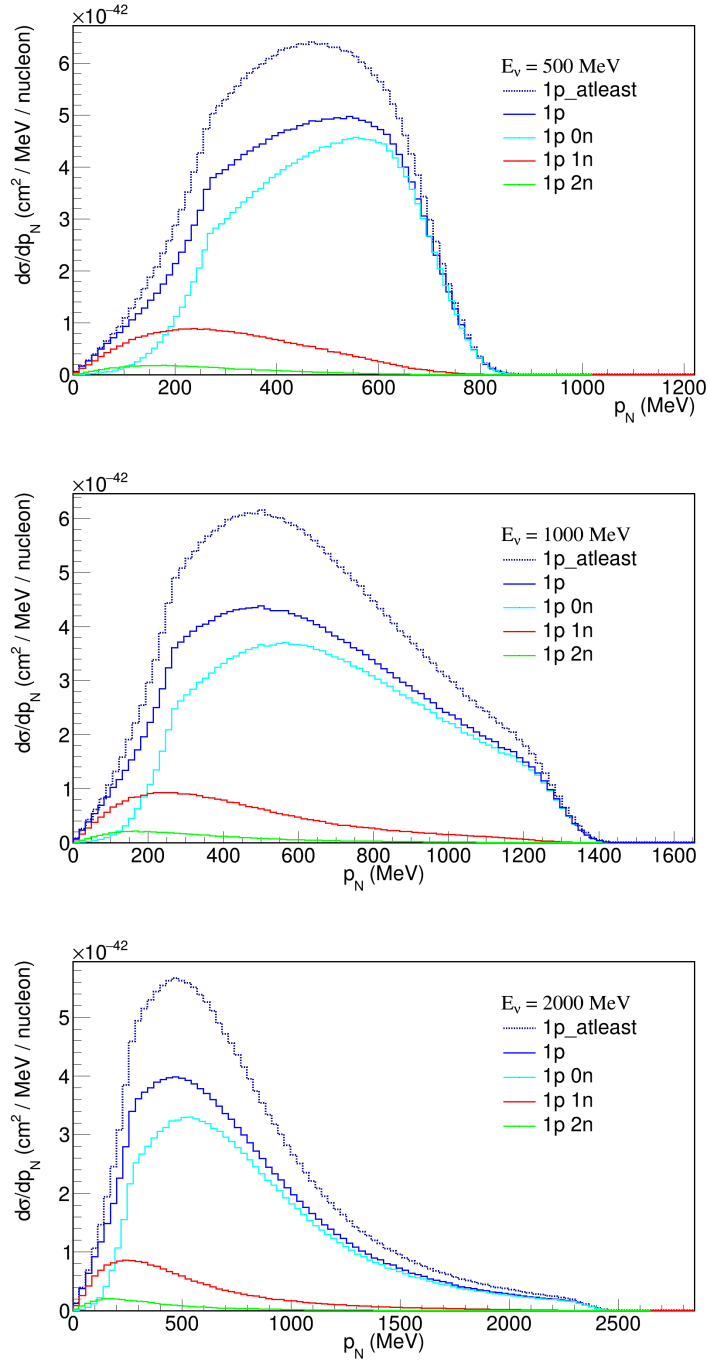
Figure 19: Single differential cross section for the breakdown of the $1p$ final state into the $0n, 1n,$ and $2n$ final states for different neutrino energy values: (top to bottom) $E_\nu = 500, 1000,$ and 2000 MeV.
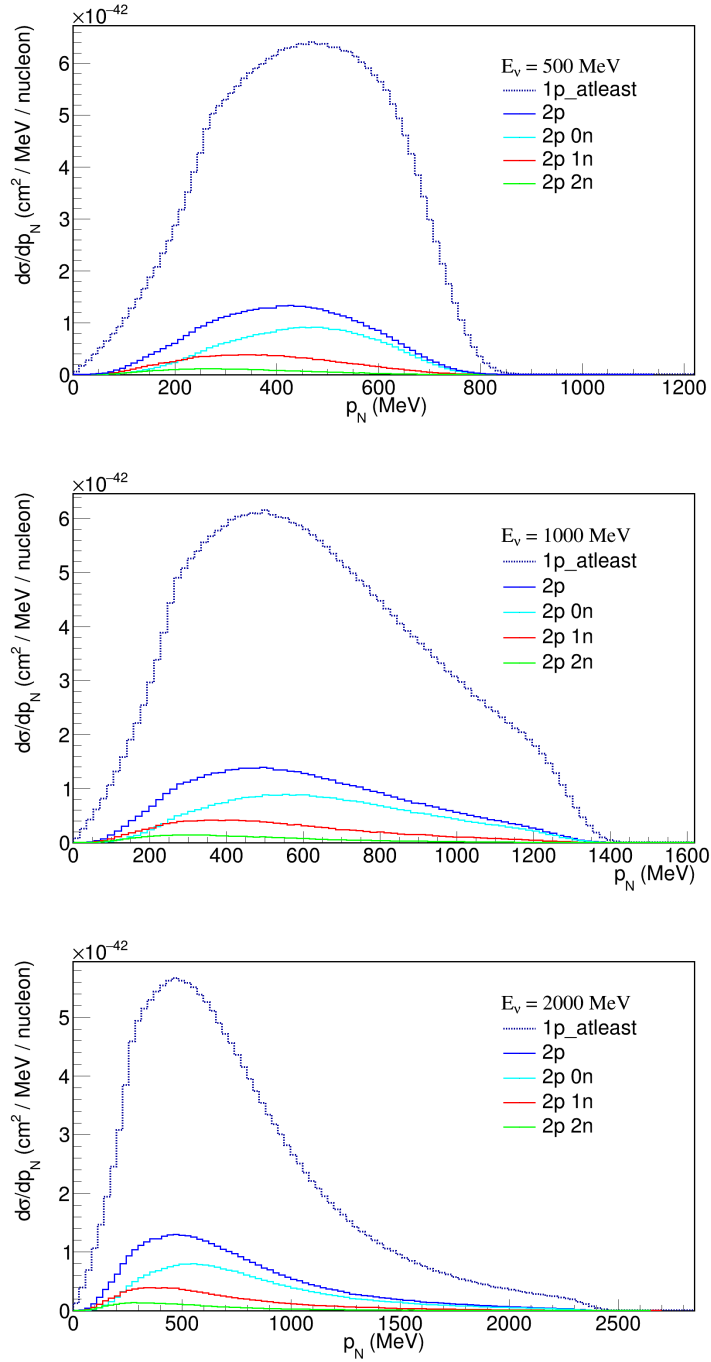
Figure 20: Single differential cross section for the breakdown of the $2p$ final state into the $0n, 1n$, and $2n$ final states for different neutrino energy values: (top to bottom) $E_\nu = 500, 1000$, and 2000 MeV.

When a proton interacts with the residual nucleus, it can lose energy enough for it to be absorbed by the nucleus due to its binding energy. The $0p$ can shed light to cases where the proton/s from the CCQE vertex can either be absorbed or be converted into a neutron as it goes through the cascade. The $0p$ state can be broken down into the $0n$, $1n$, $2n$, and $3n$ states shown in Figure 23. Because there is no proton exiting the nucleus, cross sections in Figure 23a are expressed as a function of p_N^{bef}, the leading proton momentum before being subjected to the FSI. Figure 23b are the same state but as a function of the momentum of the neutron knocked out of the nucleus. The $0p0n$ state in Figure 23a arise from low energy protons interacting with the residual system. It also represents the neutrons absorbed by the nucleus that translate as the events around $p_{neut} = 0MeV$ in the $0p$ state in Figure 23b.

It is also interesting to look at the more specific case where it is the neutron, and not the proton, that is the leading nucleon. For this purpose the $1p1n$ and the $0p1n$ states are shown in Figure 24. For simplicity, this only includes events where there is only 1 proton produced that re-interacts with the residual system. In the $1p1n$ state, higher energy protons entering the cascade result to knocking out a low energy proton and a low energy neutron whose momenta is mostly below the Fermi momentum. Same could be said for the $0p1n$ figure, where the excess in the proton before cascade curve (black line) translate to low momentum neutrons after the cascade (green line).
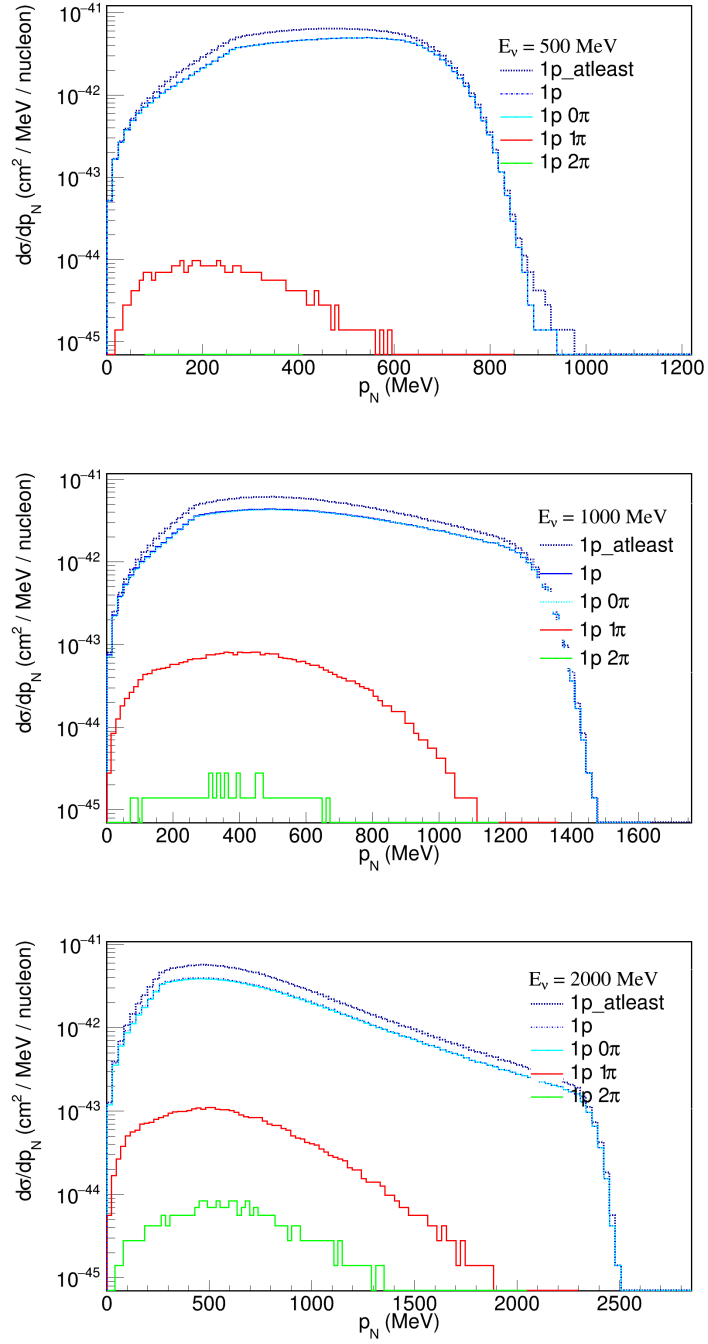
Figure 21: Single differential cross section for the breakdown of the $1p$ final state into the $0\pi, 1\pi$, and 2π final states for different neutrino energy values: (top to bottom) $E_\nu = 500, 1000$, and 2000 MeV. The y-axis is in log scale.
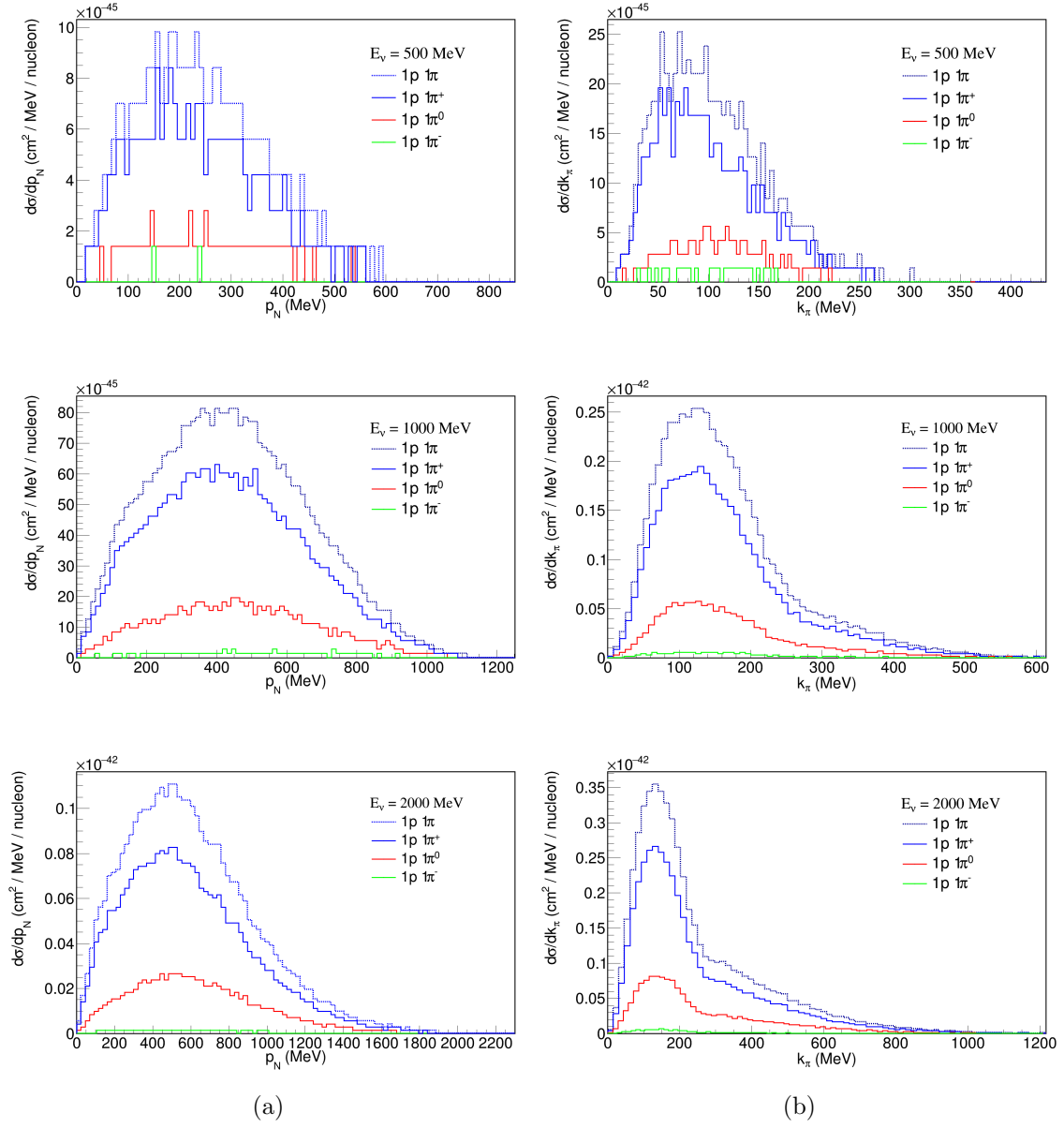
Figure 22: Single differential cross section for the breakdown of the $1p1\pi$ final state into the $1\pi^+, 1\pi^0$, and $1\pi^-$ final states for different neutrino energy values: (top to bottom) $E_\nu = 500, 1000$, and 2000 MeV. These are obtained as a function of the (a) outgoing proton momentum and as a function of the (b) pion momentum.
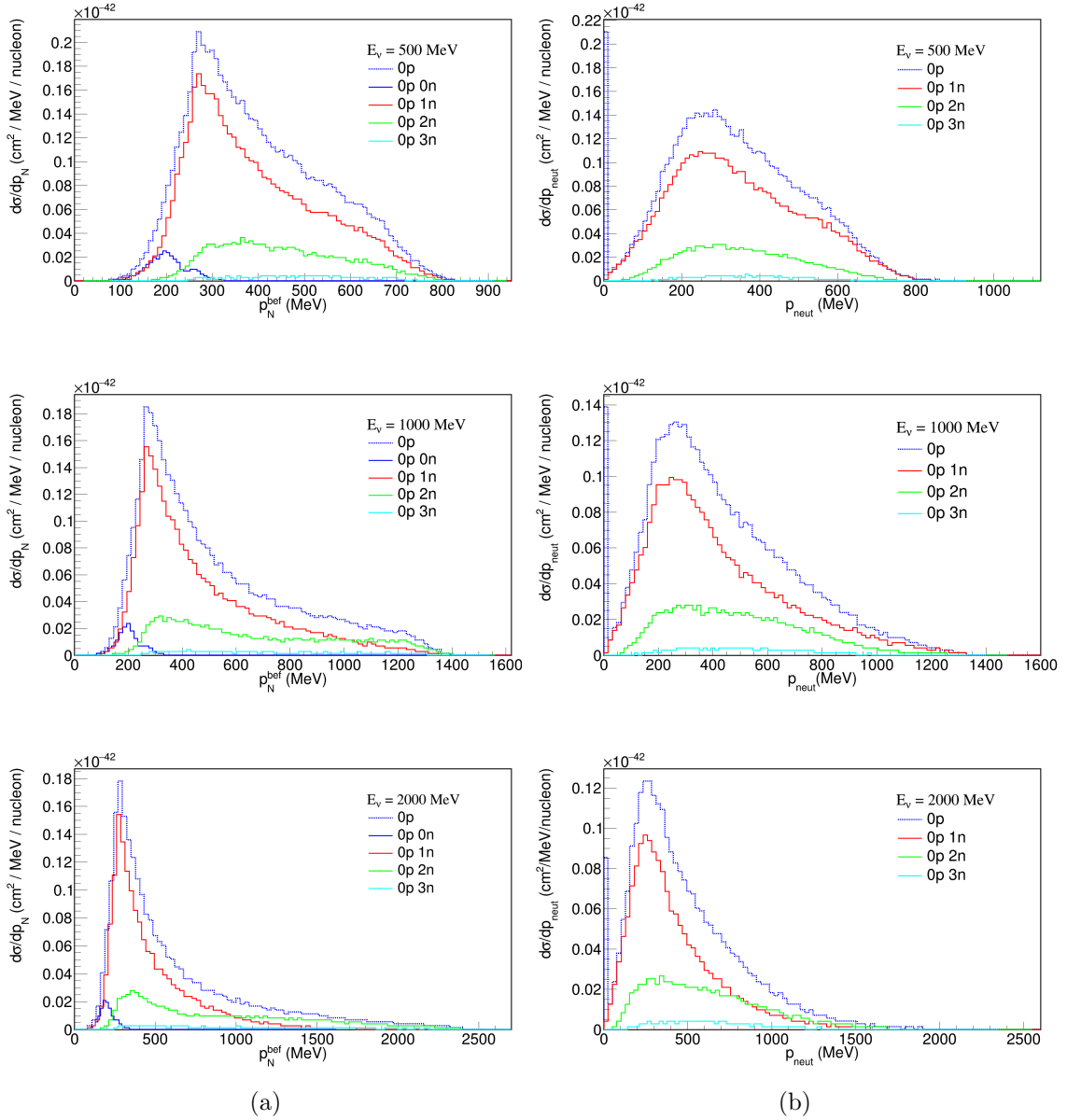
Figure 23: Single differential cross section for the breakdown of the $0p$ final state into the $0n, 1n, 2n$, and $3n$ final states for different neutrino energy values: (top to bottom) $E_\nu = 500, 1000$, and 2000 MeV. These are obtained as a function of the (a) leading proton momentum before the cascade and as a function of the (b) leading neutron momentum after the cascade
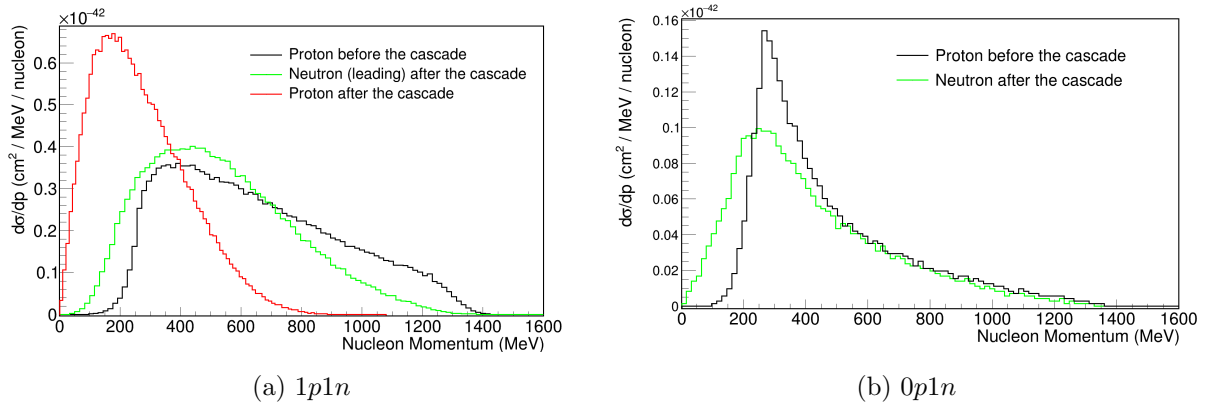
(a) $1p1n$

(b) $0p1n$

Figure 24: Comparison of the momentum spectrum of the proton before the cascade, then leading neutron and a proton after the cascade for (a) the $1p\ 1n$ final state and (b) the $0p\ 1n$ final state.

4.3.2 Comparison to Theoretical Models

Theoretical cross sections calculations can be made for different descriptions of the final state. These theoretical models used in this part of the results are described in Ref. [42]. The FSI is treated in a fully quantum relativistic mean field (RMF) framework, using different phenomenological optical potentials and solutions to the wave equation for the final nucleon. This can be compared to NuWro's simulation through the cascade model, as shown in Figure 25. The way FSI is treated for these theoretical models is different from how NuWro where the FSI is treated semi-classically where quantum effects like Pauli blocking and nucleon correlation are added to the base model. Additionally, in NuWro, the leading proton exiting the nucleus is not necessarily the same leading proton entering the cascade, although usually it is.
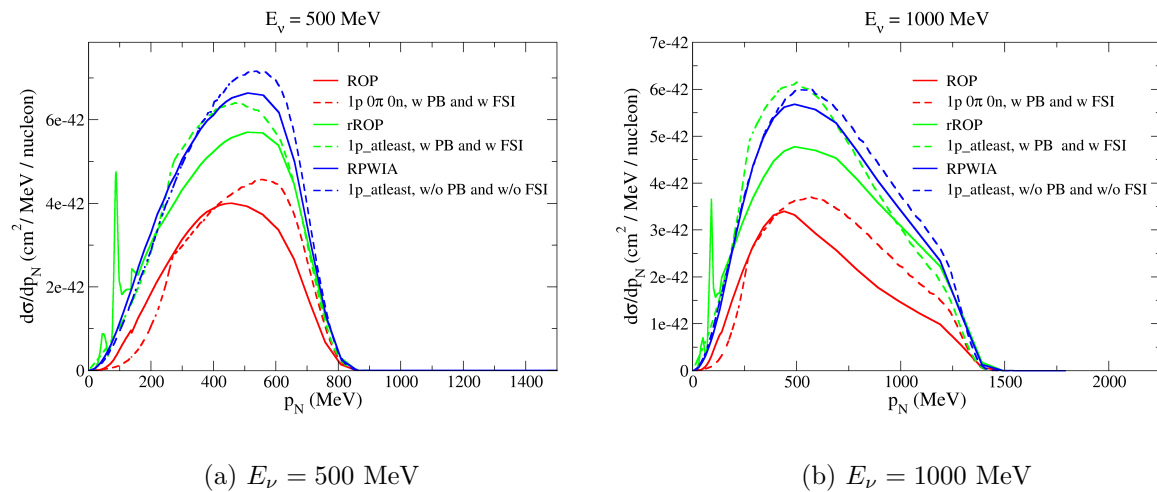
56

(a) $E_\nu = 500$ MeV

(b) $E_\nu = 1000$ MeV

Figure 25: Comparison of NuWro cross sections (broken lines) of different final state configurations and ROP, rROP, and RPWIA calculations for (a) $E_\nu = 500$ MeV and (b) $E_\nu = 1000$ MeV.

In the Real Relativistic Optical Potential (rROP) curve, the final-state nucleon is represented as a solution to the Dirac equation with a real potential (no imaginary component). In a semi-inclusive cross section calculation, this model should describe an estimate where the final state signal consists of at least one proton, that may or may not be accompanied with hadrons produced from the FSI.

Meanwhile, the Relativistic Optical Potential (ROP) reproduces the signal that represents the elastic proton-nucleus scattering in the final state interactions. Unlike rROP, this optical potential contains real and imaginary components. This describes a system where the leading nucleon is knocked out during its interaction with the exchanged boson and it interacts with the residual nucleus through elastic scattering only. So this nucleon does not knock out any other nucleons or pions in the nucleus and it does not lose energy (magnitude) along the way. This should estimate the one proton signature without any pions or other nucleons in the final state.

In the Relativistic Plane Wave Impulse Approximation (RPWIA) case, the final nucleon is a relativistic plane wave. This is combined with the assumption of IA, so the effects of FSI and PB are neglected. Tthis provides an estimation of the not-Pauli-blocked $1p\_atleast$ signal.

Overall, there seems to be a large excess in the NuWro signals around higher energies and some deficit at lower energies when compared to calculation of the described theoretical models. The differences between the NuWro final state calculations and theoretical models could arise from other sources, but the next section focuses on the differences arising from the nature of NuWro's cascade model.

4.3.3   Effects of the Cascade

For the following part of the results, the effects of the FSI on the momentum of the leading proton is studied. To simplify, only non-SRC events are considered, meaning there is only one proton produced in CCQE and that interacts with the residual system. Figure 26-28 shows the comparison between the momentum of the leading proton before the cascade and after the cascade. These figures are calculation for the neutrino energy, $E_\nu = 1000$ MeV. The corresponding theoretical calculations, as discussed earlier, are also shown for reference. These figures qualitatively show the effect of the FSI for that particular final state signal.

Figure 26 shows the $1p0\pi0n$ signal before and after the cascade. Because this signal is meant to represent the proton interacting only elastically with the residual system, the proton doesn't lose energy and the curves before and after the FSI doesn't show any difference. When compared to the the theoretical calculation, ROP, even with the removal of SRC events, there is a deficit in the NuWro calculation for lower momenta and an excess for higher values.
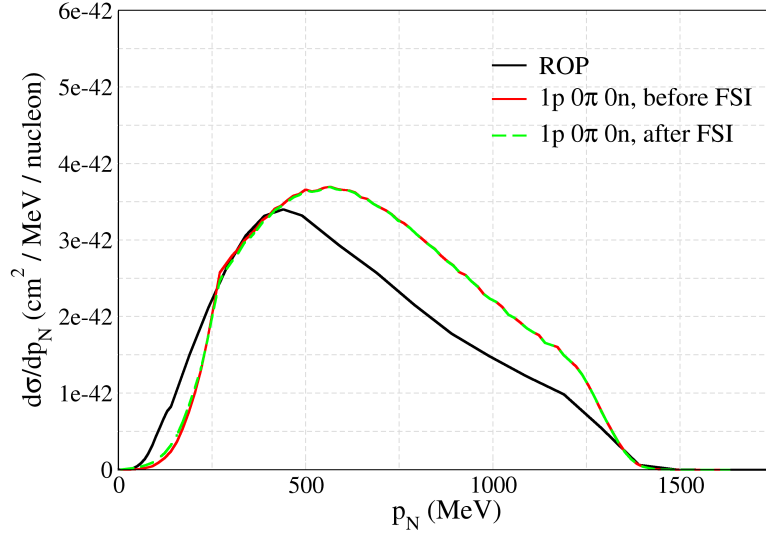
Figure 26: Before and after cascade cross sections of $1p0\pi0n$ compared with ROP. The neutrino energy is $E_\nu = 1000$ MeV.
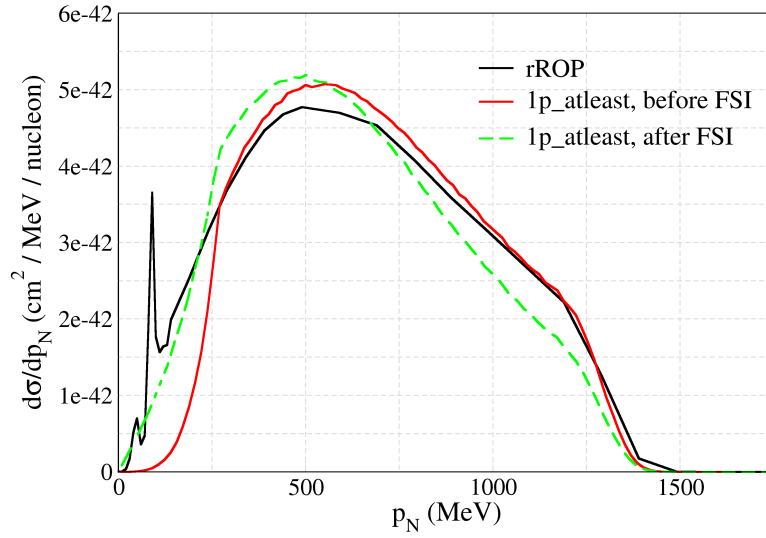

Figure 27: Before and after cascade cross sections of $1p\_atleast$ compared with rROP. The neutrino energy is $E_\nu = 1000$ MeV.

59

Figure 27 compares the 1p_atleast signal for before and after FSI. It can be said that because of the FSI the momentum spectrum of the leading proton is shifted to the right, to lower momentum values. At lower energies, the *after FSI* curve is close to the rROP curve, while it is the *before FSI* curve that is closer at higher energies. Because the 1p_atleast state include elastic events, the excess at higher momenta in Figure 26 is carried over here. This is further supported by the fact that the mismatch in the rROP comparison curve also starts at the same point where the excess in $1p0\pi0n$ events in the ROP comparison curve begins, at $p_N \sim 260$ MeV.
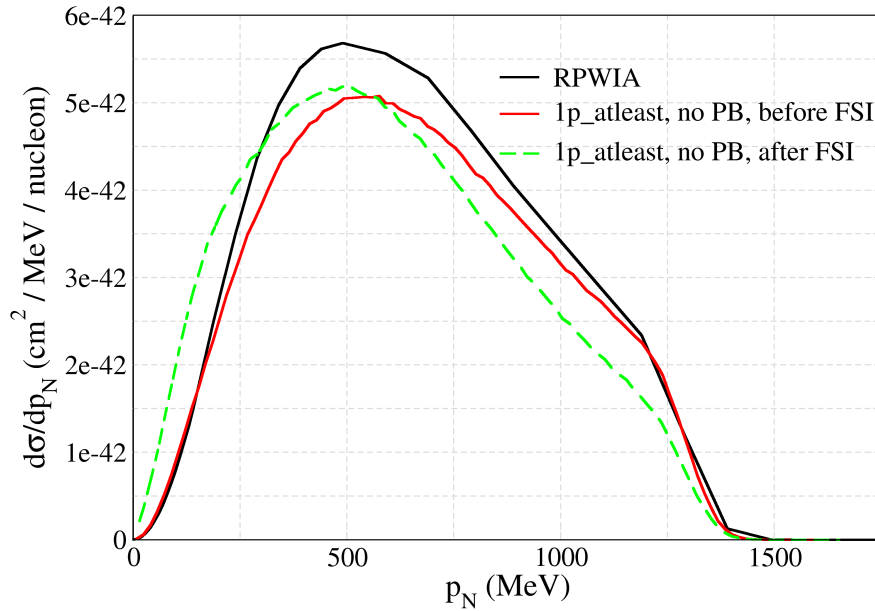

Figure 28: Before and after cascade cross sections of 1p_atleast (without PB) comparison with RPWIA. The neutrino energy is $E_\nu = 1000$ MeV.

Lastly, Figure 28 shows the before and after FSI comparison for the 1p_atleast final state, this time the PB is not implemented in the NuWro curve. As expected it is the *before FSI* curve that is closer to the RPWIA curve. When the nucleons are represented by a relativistic plane wave, the FSI effects are not accounted for.

To further show the effect of FSI, the mean leading proton momentum after the cascade is obtained for a particular leading proton momentum before the cascade, p_N^{bef}, as shown in Figure 29a. This shows how the leading proton loses more energy in the FSI for increasing pre-cascade momentum, however only start at values above 100 MeV. This increasing loss of momentum also translates as an increase in the energy of a new secondary proton produced in the cascade, further shown in Figure 29b. It is evident here that not all of the loss of momentum in the leading proton goes to the energy of the new second proton. This is attributed to other products of inelastic channels in the FSI.

Figure 30 shows the mean number of protons coming out of the nucleus as a function of the proton momentum before the cascade, p_N^{bef}. This value is obtained through averaging the number of protons coming out of the nucleus, after FSI, among all events. At $p_N^{\mathrm{bef}} <$ 220 MeV, there is very little possibility to knockout an additional proton, which means in the majority of these events, the original proton undergoes only elastic scattering. Also, at a range of 100 MeV $< p_{\mathrm{bef}}^N <$ 220 MeV, there is a significant number of events where the proton is absorbed by the nucleus, where the mean number of protons has a value a little below 1.

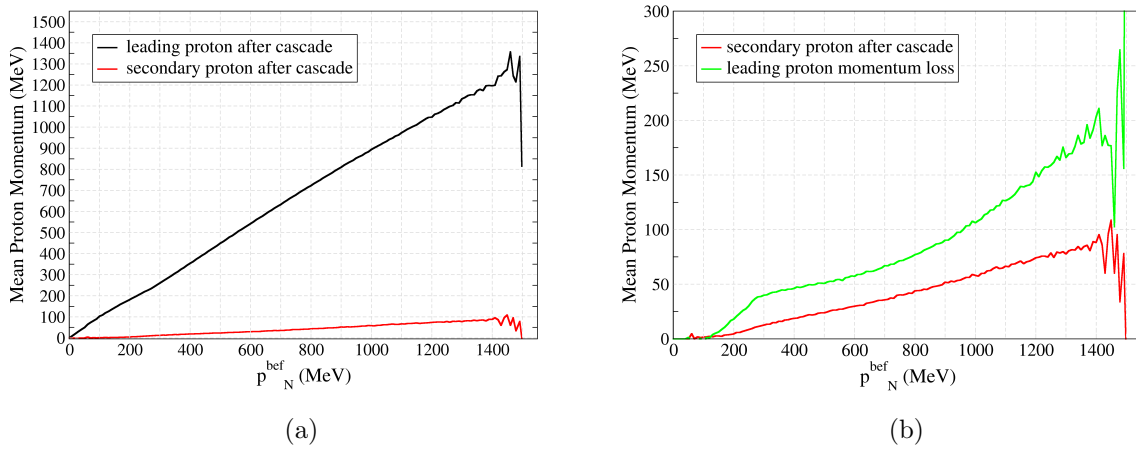(a)   (b)

Figure 29: (a) Mean proton momentum after the cascade vs the momentum before the cascade, for both the leading proton and the secondary proton produced after FSI. (b) Comparison of the momentum of the secondary proton with the momentum lost by the leading proton.
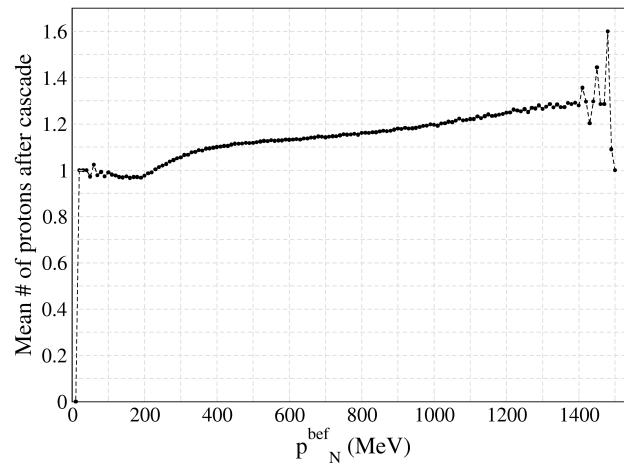

Figure 30: Number of protons emerging from nucleus after FSI as a function of the momentum of the single proton produced at the CCQE vertex

To look at the overall picture, Figure 31 shows different final states for the proton momentum before and after the FSI compared with the previous ROP and rROP curves. Figure 31a shows which parts of the momentum spectra of the singular proton before the cascade result to a particular final state. Notable curves are the 1π final state that require higher proton momenta. The $1p0\pi0n$ state can be considered the elastic channel of the final state interactions, and it can be seen that it occupies most of the spectra at lower energies. Final states that could point to inelastic interactions in the cascade only begin to have events at momenta approximately above 220 MeV.

Figure 31b shows the momentum distribution of the leading proton after the FSI for different final states. Most of the curves show that the FSI shifts the proton momentum to the right hence to lower values, except for the elastic $1p0\pi0n$ curve. Additionally, the $0p$ curve represent the protons absorbed by the nucleus, where low energy protons before the FSI have zero momentum after the FSI. Other observations could be made of, say, the 1π state, among all states, features a very far shift of the proton momentum to low values. Particularly, the mean momentum is reduced to 450 MeV from 1060 MeV. This further supports the behavior described earlier where at higher pre-cascade proton momenta, the more the proton loses energy. This highlights the significance of inelastic channels in the FSI at higher proton energies.
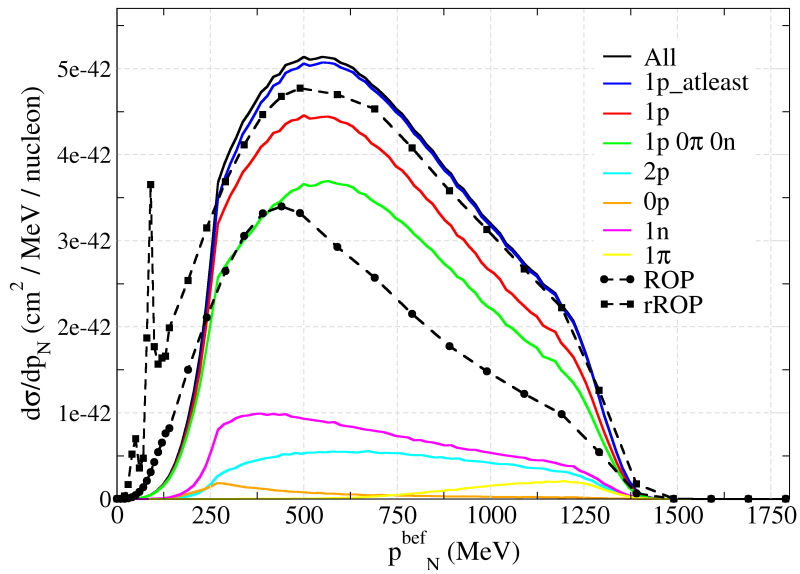
(a) Before FSI
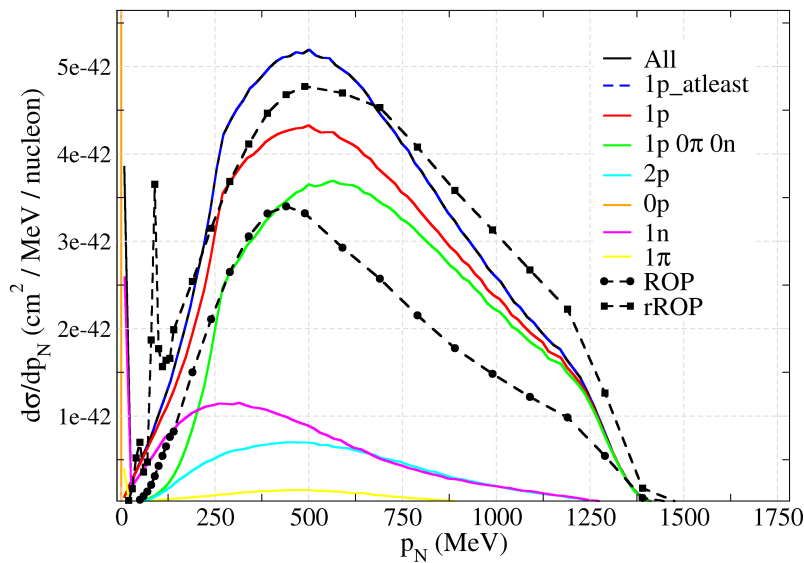
(b) After FSI

Figure 31: (a) Single differential cross section of *All* non-SRC events, where there is only one proton entering the cascade. Curves for possible final states are shown as a function of p_N^{bef}, momentum of the proton before FSI. (b) Same final states shown, this time as a function of p_N, the momentum of the leading proton after FSI.

64

5 Conclusions

In summary, the different cross sections were numerically calculated for two different nuclear models, RFG and SF, and were compared with each other. The agreement between these two models is further improved by incorporating the binding into the RFG model. Data from the T2K experiment on the neutrino flux was also incorporated into the calculation through the flux-folded case. Differential cross section curves were also obtained as a function of neutrino energy, for both the no flux and flux-folded case. These calculations were compared to that of NuWro's. The RFG model can be implemented in NuWro in two ways. The global FG is found to implement Pauli Blocking effect but features an unphysical cut at initial nucleon momenta higher than the Fermi momentum, $p_F = 220$ MeV. This is due to the fact this mode featured a constant Fermi momentum distribution independent of the nuclear density. The LFG model fixes this by using a p_F distribution dependent on the nuclear density. This model is able to reproduce the low momentum tail in the cross section curve of the initial nucleon momentum, p, that is also seen in the SF model in NuWro. When compared overall, it is NuWro's SF model that is closest to the numerical RFG and SF cross section magnitudes. NuWro's SF was able to reproduce the expected high p_N tail in the cross section.

Further into the study, the final-state nucleon was examined. This final state is what is detected in the experiment, so only looking at nuclear models for the initial nucleon momentum is not enough, final state interactions must also be considered. The final state was broken down into different possibilities and for three different neutrino energies, $E_\nu = 500, 1000, 2000$ MeV. This breakdown gave insight to how much of the total $1p\_atleast$ final state are from contributions of other final state configurations. The $1p\_atleast$ state means that the final state involves one or more protons knocked out of the nucleus. The state ip meant there is i number of protons, that could be accompanied by pions or neutrons or nothing else. The $1p$ state was shown to be the major contributing channel

compared to the $0p$, $2p$, $3p$ final states. This final state includes elastic and inelastic reactions, but as shown by the cross sections of the $1p$ jn or $1p$ $j\pi$, where $j \geq 1$, the inelastic reactions contribute way less than the elastic channel.

The final-state nucleon can be characterized analytically by treating the FSI quantum mechanically. Models like rROP, ROP, and RPWIA use a combination of different optical potentials and wave equation solutions to represent different final state configurations. This was compared to different final states simulated by NuWro. To determine the cause of the differences between theory and NuWro, the cascade model was explored. In the $1p0\pi0n$ state, the cascade does not cause any significant effect. This state was supposed to reflect the case where the proton only interacts elastically with the residual system; however, NuWro has a deficit of events in lower momenta while an excess at higher energies when compared to the ROP model. Meanwhile, the NuWro simulation of the $1p\_atleast$ after FSI should match the rROP curve. It was found to only do that at lower energies. At higher energies, it was the *before FSI* signal that is closer to the rROP. This mismatch at higher momenta can be attributed to the excess of the elastic $1p0\pi0n$ signal, pointing to an area where the NuWro cascade model could improve on.

Finally, the study showed which parts of the momentum spectra of the proton entering the cascade result to a particular final state. The elastic channel, as reflected in the $1p0n0\pi$ curve, fully takes up the lower momentum region, while the final states that are produced by inelastic channels only start to get events at momenta above the 220 MeV. These events are then plotted for after the FSI and numerous observations were made.

As a recommendation, further and more quantitative study could be made of NuWro's cascade at particular final states.

References

[1] A Ereditato. *The State of the Art of Neutrino Physics*. WORLD SCIENTIFIC, 2018. DOI: 10.1142/10600. eprint: https://www.worldscientific.com/doi/pdf/10.1142/10600.

[2] H Bethe and R Peierls. "The Neutrino". In: *Nature* 133 (1934), p. 532. DOI: 10.1038/133532a0.

[3] B Pontecorvo et al. *Bruno Pontecorvo selected scientific works: recollections on Bruno Pontecorvo; 2nd ed.* Bologna: SIF, 2013.

[4] CL Cowan et al. "Detection of the Free Neutrino: a Confirmation". In: *Science* 124.3212 (1956), pp. 103–104. DOI: 10.1126/science.124.3212.103.

[5] N Majorana. "A symmetric theory of electrons and positrons". In: *Ettore Majorana Scientific Papers: On occasion of the centenary of his birth* (2006), pp. 201–233. DOI: 10.1007/978-3-540-48095-2_10.

[6] M Aker et al. "Analysis methods for the first KATRIN neutrino-mass measurement". In: *Physical Review D* 104.1 (2021), p. 12005. ISSN: 2470-0029. DOI: 10.1103/PhysRevD.104.012005. arXiv: 2101.05253.

[7] M Schwartz. "Feasibility of Using High-Energy Neutrinos to Study the Weak Interactions". In: *Phys. Rev. Lett.* 4 (6 Mar. 1960), pp. 306–307. DOI: 10.1103/PhysRevLett.4.306.

[8] KA Olive. "Review of Particle Physics". In: *Chinese Physics C* 38.9 (Aug. 2014), p. 90001. DOI: 10.1088/1674-1137/38/9/090001.

[9] K Kodama et al. "Observation of tau neutrino interactions". In: *Phys. Lett. B* 504 (2001), pp. 218–224. DOI: 10.1016/S0370-2693(01)00307-0. arXiv: 0012035 [hep-ex].

[10]   Z Maki, M Nakagawa, and S Sakata. "Remarks on the unified model of elementary particles". In: *Prog. Theor. Phys.* 28 (1962), pp. 870–880. DOI: 10.1143/PTP.28.870.

[11]   QR Ahmad et al. "Measurement of the Rate of $\nu_e + d \to p + p + e^-$ Interactions Produced by ^8B Solar Neutrinos at the Sudbury Neutrino Observatory". In: *Phys. Rev. Lett.* 87 (7 July 2001), p. 071301. DOI: 10.1103/PhysRevLett.87.071301.

[12]   K Eguchi et al. "First Results from KamLAND: Evidence for Reactor Antineutrino Disappearance". In: *Phys. Rev. Lett.* 90 (2 Jan. 2003), p. 021802. DOI: 10.1103/PhysRevLett.90.021802.

[13]   K Abe et al. "Constraint on the matter–antimatter symmetry-violating phase in neutrino oscillations". In: *Nature* 580.7803 (2020), pp. 339–344. ISSN: 14764687. DOI: 10.1038/s41586-020-2177-0. arXiv: 1910.03887.

[14]   F Detector and T Design. "Deep Underground Neutrino Experiment (DUNE) Far Detector Technical Design Report". In: I.January (2020). arXiv: arXiv:2002.02967v3.

[15]   L Alvarez-Ruso et al. "NuSTEC White Paper: Status and challenges of neutrino–nucleus scattering". In: *Progress in Particle and Nuclear Physics* 100 (2018), pp. 1–68. ISSN: 01466410. DOI: 10.1016/j.ppnp.2018.01.006. arXiv: 1706.03621.

[16]   TV Cuyck. "Short-range correlations and meson-exchange currents in neutrino-nucleus scattering." PhD Thesis. Universiteit Gent, 2017.

[17]   H Dinh, JM Udias, and R González-Jiménez. "Nuclear Effects in Energy Reconstruction for Neutrino Oscillation Experiments". Master's Thesis. Universidad Complutense de Madrid, 2020.

[18]   W Greiner, J Reinhardt. *Quantum Electrodynamics 3rd Ed.*

[19]   AM Ankowski and JT Sobczyk. "Construction of spectral functions for medium-mass nuclei". In: *Physical Review C - Nuclear Physics* 77.4 (2008), pp. 1–14. ISSN: 1089490X. DOI: 10.1103/PhysRevC.77.044311.

[20]   TW Donnelly et al. *Foundations of Nuclear and Particle Physics*. Cambridge University Press, pp. 477–505. ISBN: 9780521765114.

[21]   JW Van Orden and TW Donnelly. "Nuclear theory and event generators for charge-changing neutrino reactions". In: *Physical Review C* 100.4 (2019), p. 44620. ISSN: 24699993. DOI: 10.1103/PhysRevC.100.044620.

[22]   O Benhar et al. "Electron- and neutrino-nucleus scattering in the impulse approximation regime". In: *Phys. Rev. D* 72 (5 Sept. 2005), p. 053005. DOI: 10.1103/PhysRevD.72.053005.

[23]   T Golan. "Modeling nuclear effects in NuWro Monte Carlo neutrino event generator". PhD Thesis. University of Wroclaw, 2014.

[24]   GT Garvey et al. "Recent advances and open questions in neutrino-induced quasi-elastic scattering and single photon production". In: *Physics Reports* 580 (2015), pp. 1–45. ISSN: 03701573. DOI: 10.1016/j.physrep.2015.04.001.

[25]   E Oset and LL Salcedo. "Delta self-energy in nuclear matter". In: *Nuclear Physics* 468 (1987), pp. 631–652.

[26]   E Oset, LL Salcedo, and D Strottman. "A Theoretical Approach to Pion Nuclear Reactions in the Resonance Region". In: *Phys. Lett. B* 165 (1985), pp. 13–18. DOI: 10.1016/0370-2693(85)90681-1.

[27]   CW De Jager, H De Vries, and C De Vries. "Nuclear charge- and magnetization-density-distribution parameters from elastic electron scattering". In: *Atomic Data and Nuclear Data Tables* 14.5 (1974), pp. 479–508. ISSN: 0092-640X. DOI: https://doi.org/10.1016/S0092-640X(74)80002-1.

REFERENCES

[28] C Andreopoulos et al. "The GENIE neutrino Monte Carlo generator". In: *Nuclear Instruments and Methods in Physics Research Section A: Accelerators, Spectrometers, Detectors and Associated Equipment* 614.1 (Feb. 2010), pp. 87–104. ISSN: 0168-9002. DOI: 10.1016/j.nima.2009.12.009.

[29] O Buss et al. "Transport-theoretical description of nuclear reactions". In: *Physics Reports* 512.1 (2012), pp. 1–124. ISSN: 0370-1573. DOI: https://doi.org/10.1016/j.physrep.2011.12.001.

[30] K Gallmeister, U Mosel, and J Weil. "Neutrino-induced reactions on nuclei". In: *Phys. Rev. C* 94 (3 Sept. 2016), p. 035502. DOI: 10.1103/PhysRevC.94.035502.

[31] Y Hayato. "Neut". In: *Nuclear Physics B - Proceedings Supplements* 112.1 (2002), pp. 171–176. ISSN: 0920-5632. DOI: https://doi.org/10.1016/S0920-5632(02)01759-0.

[32] T Golan, JT Sobczyk, and J Zmuda. "NuWro: The wrocław monte carlo generator of neutrino interactions". In: *Nuclear Physics B - Proceedings Supplements* 229-232 (2012), p. 499. ISSN: 09205632. DOI: 10.1016/j.nuclphysbps.2012.09.136.

[33] C Juszczak, JA Nowak, and JT Sobczyk. "Simulations from a new neutrino event generator". In: *Nuclear Physics B - Proceedings Supplements* 159.1 (2006), pp. 211–216. ISSN: 09205632. DOI: 10.1016/j.nuclphysbps.2006.08.069.

[34] *GitHub - NuWro/nuwro: The main distribution of NuWro.* https://github.com/NuWro/nuwro. (Accessed on 09/03/2021).

[35] N Metropolis et al. "Monte Carlo Calculations on Intranuclear Cascades. I. Low-Energy Studies". In: *Phys. Rev.* 110 (1 Apr. 1958), pp. 185–203. DOI: 10.1103/PhysRev.110.185.

[36] SK Singh and E Oset. "Inclusive quasielastic neutrino reactions in ^{12}C and ^{16}O at intermediate energies". In: *Phys. Rev. C* 48 (3 Sept. 1993), pp. 1246–1258. DOI: 10.1103/PhysRevC.48.1246.

[37] TS Kosmas and E Oset. "Charged current neutrino-nucleus reaction cross sections at intermediate energies". In: *Phys. Rev. C* 53 (3 Mar. 1996), pp. 1409–1415. DOI: 10.1103/PhysRevC.53.1409.

[38] D Dutta, K Hafidi, and M Strikman. "Color transparency: Past, present and future". In: *Progress in Particle and Nuclear Physics* 69 (2013), pp. 1–27. ISSN: 0146-6410. DOI: https://doi.org/10.1016/j.ppnp.2012.11.001.

[39] K Niewczas and JT Sobczyk. "Nuclear transparency in Monte Carlo neutrino event generators". In: *Physical Review C* 100.1 (2019), pp. 1–9. ISSN: 24699993. DOI: 10.1103/PhysRevC.100.015505. arXiv: 1902.05618.

[40] C Patrignani et al. "Review of Particle Physics". In: *Chin. Phys. C* 40.10 (2016), p. 100001. DOI: 10.1088/1674-1137/40/10/100001.

[41] *INCL - the Liège Intranuclear Cascade model.* http://irfu.cea.fr/dphn/Spallation/incl.html. (Accessed on 09/10/2021).

[42] R González-Jiménez et al. "Neutrino energy reconstruction from semi-inclusive samples". In: 3 (2021), pp. 1–19. arXiv: 2104.01701.